1 content of this file

1. Supplementary Text 1 to 5

2. Supplementary Figures 1 to 21

3. Supplementary Tables 1 to 9

2 Introduction

This file contains 5 Supplementary Texts, 21 Supplementary Figures and 9 Supplementary Tables. Supplementary texts S1 to S3 give further details on the rift detection and measurement workflow described in Sect. 3.1. Text S1 gives additional details of filtering applied to minimize erroneous rift wall detections, Text S2 describes the assignment of a confidence level to individual rift measurements, of particular relevance where the rift is bisected by an ice block and two measurements must be combined to calculate an "opening width" (see also Fig. S4). The combining of bisected rift measurements is discussed in Text S3. Text S4 discusses the production of a Digital Elevation Model (DEM) of Brunt Ice Shelf (BIS) using SlideRule ICESat-2 data. Text S5 discusses the *icepack* finite element ice flow modeling.

Fig. S1 shows the surface velocity field of BIS and the grounded ice immediately upstream in 2015, prior to the initiation of Halloween Crack (HC) (velocity data generated using auto-RIFT (Gardner et al., 2018) and provided by the NASA MEa-SUREs ITS_LIVE project (Gardner et al., 2020)). The pinning point at McDonald Ice Rumples (MIR) can be seen to exert a strong control on ice shelf flow in the vicinity of the tips of Chasm 1, HC and North Rift (NR). The flow field can be seen to be discontinuous across Chasm 1, reflecting the widening of this rift. The locations of the four Global Navigation Satellite Systems (GNSS) receivers are shown, together with their flow velocity, and the rift-perpendicular component of flow velocity. The rift-perpendicular flow velocities are used to calculate ice flow divergence between the two receivers of each GNSS pair, and subtracted from the rift-perpendicular separation distance time series, providing a better approximation of the HC opening rate that would be measured by GNSS receivers placed close to the rift walls. This is compared to rift widths from ICESat-2 and digitized satellite imagery in Figs. 4, 5 and 6.

Fig. S2 shows HC digitized on a Landsat-8 OLI image from 2020-02-20 (Landsat image courtesy U.S. Geological Survey), the location of the four GNSS receivers used in this study as of 2018-02-15 (and an additional unused GNSS receiver), and the center of the nadir beam pair of the 17 ICESat-2 reference ground tracks (RGTs) which yield HC width estimates (see Table 1). Fig. S3 shows the movement of the GNSS receivers, and alignment and location of the RGTs, justifying the selection of those used. RGT 215 1LR and RGT 1160 3LR are approximately aligned with the western GNSS pair; RGT 786 2LR is oblique to the western GNSS pair, but measures a similar part of the rift; RGT 283 1LR and RGT 725 3LR are approximately aligned with the eastern GNSS pair; RGT 1099 2LR is oblique.

It can be seen in Fig. S3 that the western and eastern ends of HC differ in their characteristics. In the west the rift is wider and generally straight, with occasional large (semi-)detached ice blocks bisecting it (Fig. S4). In the east the rift is not as wide and exhibits a degree of meandering. Thus, width estimates from ICESat-2 or digitization of WorldView-1-3/Landsat-8 satellite images corrected for large-scale ($\sim$10 km) rift orientation are accurate in the west (Fig. 4), but are prone to overestimation in the east where the RGT occasionally aligns with a small-scale ($\sim$1 km) meanders (Fig. 5).

Fig. S4 shows the division of the rift by a large detached ice block, manifesting in the ICESat-2 ATL06 data as two separate troughs. Fig. S5 shows the origin of these isolated blocks and icebergs through the rift initiation and widening processes, and demonstrates why, when the blocks remain largely *in situ*, the "opening width" is the appropriate measurement to use in comparing rift width measurements from ICESat-2, Landsat-8 and WorldView-1-3 satellite imagery with GNSS receiver separation for the purpose of ICESat-2 rift width measurement algorithm validation in Figs. 4 and 5. Tables S3 and S6 record both "opening width" and "wall-to-wall" width. Fig. S6 shows how small-scale meanders can lead to overestimation of rift width. Underestimation could also occur in meandering areas of the rift due to shear.

The ICESat-2 measurements used in Figs. 4 and 5 are shown in Figs. S7 to S14. Figs. S7 and S8 show detections along RGT 215 1LR, Fig. S9 along RGT 1160 3LR, Figs. S10 and S11, along RGT 786 2LR, Fig. S12 along RGT 283 1LR, Fig. S13 along RGT 725 3LR, and Fig. S14 along RGT 1099 2LR. High confidence detections are shown in light red, five lower con-

fidence detections (light orange) of small parts of the rift separated from the main rift by (semi-)detached ice blocks, and combined with the high confidence detections to calculate the "opening width" are shown in Figs. S9i, S9j, S11c, S11i and S12a. Width measurements along RGT 215 1LR on 2019-07-12 (Fig. S7d–f), along RGT 1160 3LR on 2018-12-13 (Fig. S9b–c), along RGT 786 2LR on 2018-11-19 and 2019-02-17 (Fig. S10a–f), along RGT 283 1LR on 2018-10-17 (Fig. S12a–c), along RGT 725 3LR on 2018-11-15 (Fig. S13a–c), and along RGT 1099 2LR on 2019-03-10 (Fig. S14a–c) were not used in

50 Figs. 4 and 5 due to satellite pointing errors.

The ICESat-2 rift width/opening rate measurements - and by extension the rift measurement algorithm - are validated using digitized rift width measurements using satellite imagery and the divergence-corrected separation of two pairs of GNSS receivers (Figs. 4, 5, 6). Whilst the ICESat-2 RGTs along which rift width is measured using ICESat-2 and digitized satellite imagery are fixed in space (Eulerian frame of reference), HC and the GNSS receivers are moving with ice flow (Figs. 1 and

55 S1) largely east to west. The rift parallel (and approximately ICESat-2-RGT-perpendicular) component of velocity near the GNSS pair baselines varies from $\sim$700 to $\sim$1000 $\mathrm{m\,a^{-1}}$ depending on location and time (as ice flow accelerates following calving from NR), according to the modeled velocity fields. Fig. S15 shows modeled HC opening rate ($\mathrm{m\,a^{-1}}$) with different flow law parameters and assumptions on location of maximum opening. It shows the difference in opening rate for locations approximating the western and eastern GNSS pair baselines, and points 1 km upstream, showing the potential effect of ice

60 flow on the comparison between the three independent rift width measurement datasets. In all cases the opening rate 1 km upstream is within 10 $\mathrm{m\,a^{-1}}$ of that at the GNSS locations. It therefore does not qualitatively effect our comparison of the three datasets. However, we note that the difference can become important closer to the rift tip(s), over long time periods, or where the displacement of ice perpendicular to the ICESat-2 RGTs over the period under consideration is a significant proportion of the rift length.

65 Fig. S16 shows the ice thickness (a–c) and ice velocity (g–i) inputs to the *icepack* ice flow models for "pre-calving", "calving" and "post-calving" periods. The thickness DEM is explained in more detail in Text S4. The feature-tracking workflow within ESA's SeNtinel Applications Platform (SNAP) was applied to pairs of Sentinel-1 SAR scenes to create the velocity maps. The change in feature-tracked flow speed and direction between the "pre-calving" period and the "calving" and "post-calving" periods is shown in h and i insets, j and k. Fig. S17 shows modeled ice velocity (a–c) and modeled fluidity parameter (f–h)

70 outputs from the inverse models for the three periods, and ice flow acceleration (d, e) between the "pre-calving" period and the "calving" and "post-calving" periods.

Figs. S18, S19, S20 and S21 show ICESat-2 elevation along RGTs which cross the calving fronts prior to and following calving from NR. We do not observe large and consistent changes in calving front freeboard (and hence ice thickness) which could explain the change in HC opening rate observed.

75 Tables S1, S2 and S5 identify the WorldView-1-3, Landsat-8 and Landsat-9 satellite images on which HC width was measured. Measurements shown are aligned with RGTs, and are corrected for the obliquity of the RGT to the rift-perpendicular plane prior to comparison with measurements from ICESat-2 and GNSS receiver separation distances in Figs. 4 and 5. Tables S3 and S6 show the "opening width" and where applicable also the "wall-to-wall" width from WorldView-1-3 and Landsat-8 imagery respectively, for RGT 215 1LR, RGT 1160 3LR and RGT 786 2LR used in Fig. 4. Tables S4 and S7 show the corresponding

80 values for RGT 283 1LR, RGT 725 3LR and RGT 1099 2LR used in Fig. 5.

Table S8 lists the Sentinel-1 SAR and Sentinel-2 and Landsat-8 optical images used in the *icepack* inverse modeling shown in Fig. 7. A feature tracking algorithm is used to extract ice flow fields from pairs of Sentinel-1 SAR images using the SeNtinel Applications Platform (SNAP). Sentinel-2 and Landsat-8 optical images are used to define the model domain. Table S9 presents the rates of HC opening for areas between the western and eastern GNSS pairs from inverse models for the "pre-

85 calving", "calving" and "post-calving" periods, and diagnostic models using modeled velocity, "pre-calving" modeled fluidity and "calving" and "post-calving" geometry (Text S5). The models were run with ice temperatures of 253 K and 260 K.

3 Text S1. Filtering

A number of filters and thresholds were applied throughout the rift detection and measurement workflow to maximise the
reliability of the rift width measurements. Each beam from each satellite pass was processed independently. Prior to rift de-
tection and measurement, any ∼4 km sections with >20 % of elevations flagged as low quality were discarded. Further, any
unrealistic elevations (>100 m) were discarded whether flagged as low quality or not. Any beams with >3 % of gaps between
elevation measurements exceeding 25 m were discarded. Rift detections were only processed if <25 % of elevations within
the expanded search area around the lowest point were flagged as low quality (Fig. 2b). If the mean separation of elevations
within each selected rift wall exceeded 50 m or there were fewer than three elevation measurements, the rift measurement
was skipped. Rift width measurements from early satellite passes with substantial pointing errors (Figs. S7d–f, S9a–c, S10a–f,
S12a–c, S13a–c, S14a–c) were not used for the validation against rift width measurements from optical satellite data and the
separation of GNSS receivers.

4 Text S2. Confidence

100 Rift detections were assigned a confidence level of "high", "medium" or "low". A potential rift was defined as any ATL06 points below 50 % of a 10 km smoothed surface. For each potential rift detection, the algorithm defined an extended search window centered on the lowest elevation point. If the elevations either side of the lowest point exceeded 80 % of the elevation of the smoothed surface, the detection was assigned a "high" confidence. If elevations on either or both sides of the rift were between 50 % and 80 % of the elevation of the smoothed surface, the detection was assigned a "medium" confidence. In the case

105 of "high" and "medium" confidence detections, the steepest slopes were found and width measured as described in Sect. 3.1. If neither threshold was satisfied, the detection was assigned a "low" confidence, and the width was defined as the extent of the ATL06 points below the 50 % of running mean threshold used for initial rift detection. Measurements based on "medium" and "low" confidence detections were discarded unless they were merged with a "high" confidence detection where the rift was bisected by an iceberg or semi-detached ice block. This ensured that rift width measurements were primarily based on

110 "high" confidence detections, but that the rift width was not frequently underestimated as a result of discarding measurements of "medium" or "low" confidence detections of generally narrow sections of the rift near the point of attachment of an ice block or recent detachment of an iceberg (Figs. S9h–i and j–k, S11b–c and h–i).

5   Text S3. Merging

Large icebergs or semi-detached ice blocks held in place by ice mélange occur at several locations along HC, originating from
the initiation of rifting (Fig. S5). If an ICESat-2 beam passes over one of these *in situ* blocks, the rift is divided into two
closely spaced troughs (Figs. S7a–f, S9d–k, S10d–f and j–l, S11a–i, S12a–c). For validation of the rift widths and rift opening
rates from ICESat-2 with measurements from GNSS receivers, it is necessary to merge the two measurements to calculate
a total "opening width" (Figs. S4 and S5). Any pair of rift measurements on the same date and along the same beam were
merged if they were separated by less than a distance limit of 500 m. The "opening width" was calculated as the sum of the
individual widths, with the "wall-to-wall" width also calculated as the distance between the most landward and most seaward
walls (Fig. S4). This distance limit was found to be sufficient for the current study, where detections of rifts other than HC are
discarded (based on a location polygon defined using multi-temporal satellite imagery), and iceberg/block widths are ∼100 m.
More advanced merging tools may be required for other ice shelves based on rift separation distance and iceberg/block size.
Medium or low confidence rift measurements (Text S2) were often narrow rift sections near the point of attachment of an
ice block to the rift wall, or the point of recent detachment of an iceberg (Figs. S9h–i and j–k, S11b–c and h–i). These were
combined with neighboring high confidence measurements as described above. Where no high confidence measurement existed
within the distance limit, the rift observation was discarded (i.e. no "opening width" measurement was a combination of two
medium or low confidence measurements, and medium or low confidence measurements which were not combined with a high
confidence measurement were discarded).

6   Text S4. Digital elevation model

The *icepack* model requires an ice shelf thickness DEM covering the entire domain. Prior to the 2021 calving from NR, BIS was advancing, and thus freely available ice shelf freeboard or thickness datasets with timestamps prior to the period of interest (2020–2021) do not cover the entire domain. We therefore used ICESat-2 data to create a new thickness DEM. We used sliderule (Swinski et al., 2022) to obtain elevation estimates derived from ICESat-2 data during the period 2020-01-01 and 2021-02-01 (immediately prior to NR calving). These were interpolated onto a regular grid, and converted to freeboard using the EGM2008 geoid model (Pavlis et al., 2012) and a mean dynamic topography estimate of -1.7 m (Andersen and Knudsen, 2009). We then extrapolated the BedMachine Antarctica (Morlighem, 2020) firn air content field to cover the domain, and subtracted it from the freeboard. Finally, we converted freeboard to thickness using an ice density of 900 $\mathrm{kg\,m^{-3}}$ and sea water density of 1027 $\mathrm{kg\,m^{-3}}$. The same thickness model is used for the "pre-calving", "calving" and "post-calving" model runs, cropping to the appropriate domain to simulate the calving of the iceberg from NR. We varied the thickness by $\pm \sim 20$ m and repeated some model runs to test the impact of thickness uncertainty, finding little change in the modeled rate of HC opening.

7 Text S5. Ice flow model

We conducted *icepack* model runs additional to the inverse models detailed in the main manuscript to investigate the importance of changes in geometry, velocity, and fluidity. These model runs are labeled "Diagnostic$_1$" to "Diagnostic$_9$" in Table S9, and were run with ice temperatures of 253 K and 260 K. Modeled velocity (used to define ice flow into the model domains across the grounding zone, divide between BIS and SWIT, and from MIR) and fluidity field outputs from the inverse models were resampled onto regular grids and the *fill* tool in QGIS used to interpolate across rifts and extrapolate beyond the calving front. This allowed fields to be used interchangeably regardless of the advection of rifts with ice flow, or changes in calving front position. "Diagnostic$_1$" is a repeat of the "pre calving" inverse model to test the impact of resampling and interpolation on HC opening rates. Opening rates were within $\sim$10 m a^{-1} of the rates from the inverse model except for the western GNSS pair at 253 K where the rate was overestimated by $\sim$30 m a^{-1}. For model runs "Diagnostic$_2$" to "Diagnostic$_5$" ice flow into the domain and the ice shelf fluidity were kept constant and the geometry was changed to "calving" and "post-calving" geometries, with HC either in its "pre-calving" geometry (to negate the potential impact of fluidity field interpolation across the rift) or in its corresponding "calving"/"post-calving" geometry. In all cases the modeled HC opening rate remained close to "pre-calving" rate, in contrast to the observations from ICESat-2, satellite imagery, and GNSS receiver separation, and the "calving" and "post-calving" inverse models. This shows that additional changes resulting from the geometry change are necessary to explain the observed pattern of HC opening. For model runs "Diagnostic$_6$" to "Diagnostic$_9$" only the "pre-calving" modeled fluidity was held constant. "Calving" and "post-calving" ice shelf geometries were used, and runs repeated with the HC in the corresponding geometry or "pre-calving" geometry as discussed above. "Calving" and "post-calving" modeled velocity was used as input at the domain boundaries. In these models the observed pattern of a decrease of HC opening rate approaching stagnation immediately after calving, before a return to opening is replicated, though with some offsets between the results from the inverse and "Diagnostic" models, particularly in the "post-calving" period. This maybe due to uncertainties introduced by the resampling and interpolation, though may also reflect the impact of changes in the fluidity field of the wider ice shelf (which likely show the opening of fractures close to the grounding zone). We therefore conclude that the changes in HC opening rate result from changes in BIS geometry following calving from NR, and the resulting reorganisation of ice flow, though additional fracturing, manifesting as increases in fluidity may play a secondary role.
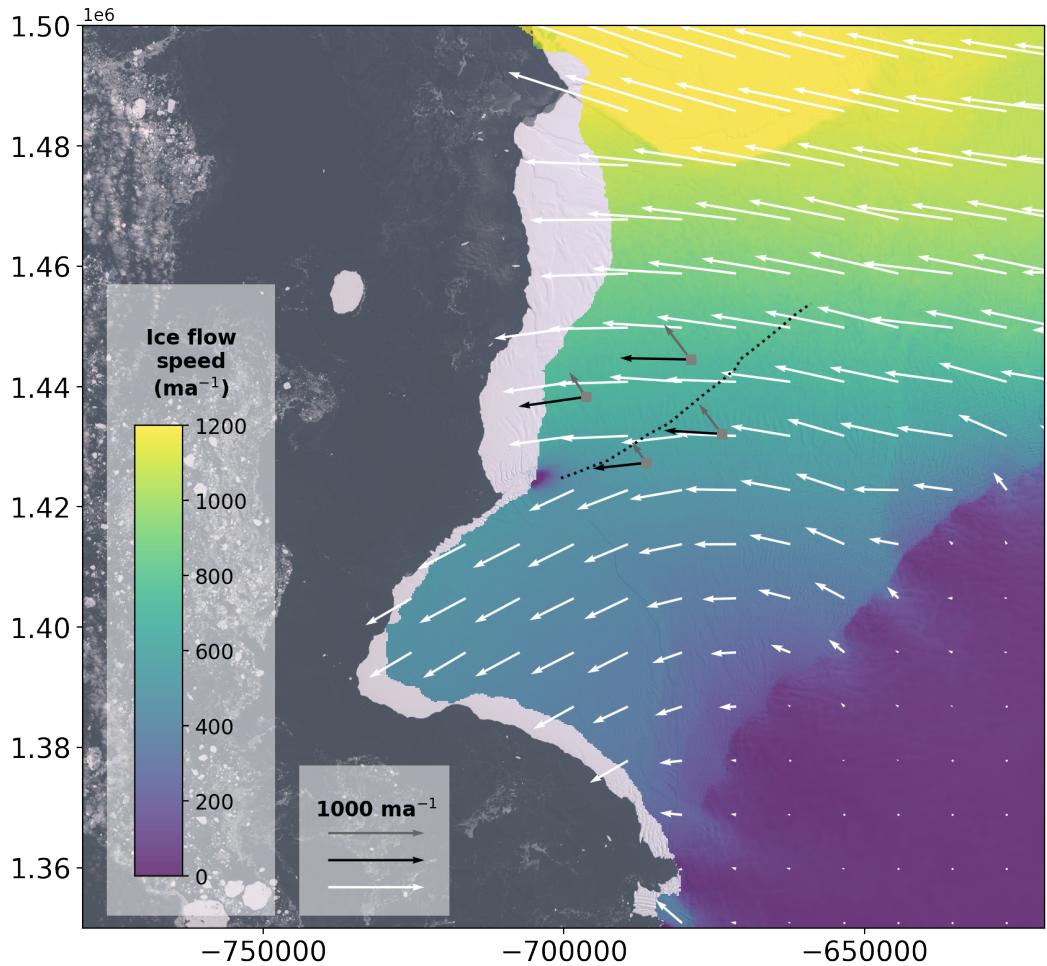
Figure 1. Brunt Ice Shelf surface flow speed field in 2015, prior to HC initiation, using velocity data generated using auto-RIFT (Gardner et al., 2018) and provided by the NASA MEaSUREs ITS_LIVE project (Gardner et al., 2020). Note the impact on the flow field of the pinning point at McDonald Ice Rumples. The black dashed line shows the large-scale axis of HC, gray squares show the mean location of the GNSS receivers, white arrows show the direction and magnitude of ice flow, black arrows show ice flow at the locations of the GNSS receivers, gray arrows show the rift-perpendicular component of ice flow at the locations of the GNSS receivers. The rift-perpendicular components of ice flow were used to remove ice flow divergence from the time series of GNSS receiver pair separation distance used in Figs. 4, 5 and 6. Removing the divergence approximately reconstructs the time series of separation that would be measured by pairs of GNSS receivers close to the walls of HC.
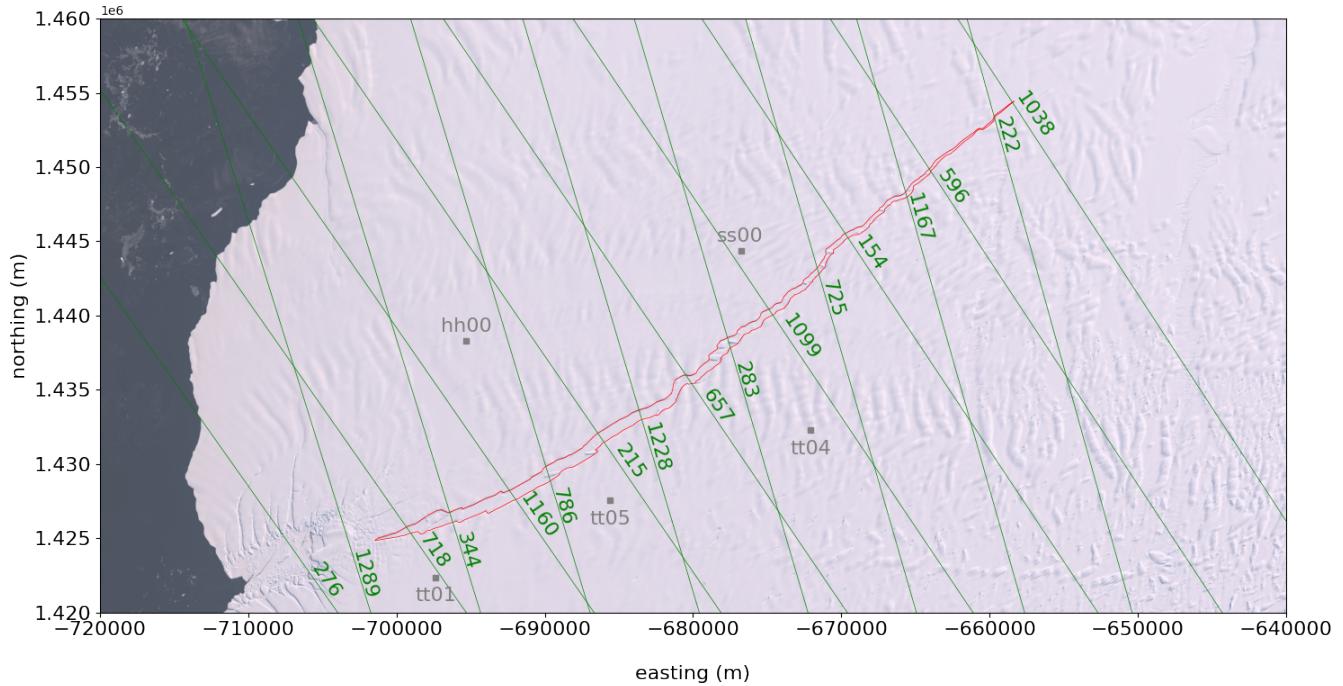
Figure 2. Centers of the nadir beam pair of 17 reference ground tracks (green, numbered), along Halloween Crack (red), on a Landsat-8 OLI image from 2020-02-20. Gray squares show the 2018-02-15 locations of the four GNSS receivers used in this study (the "western pair": hh00 and tt05, and the "eastern pair": ss00 and tt04) and unused GNSS receiver tt01.
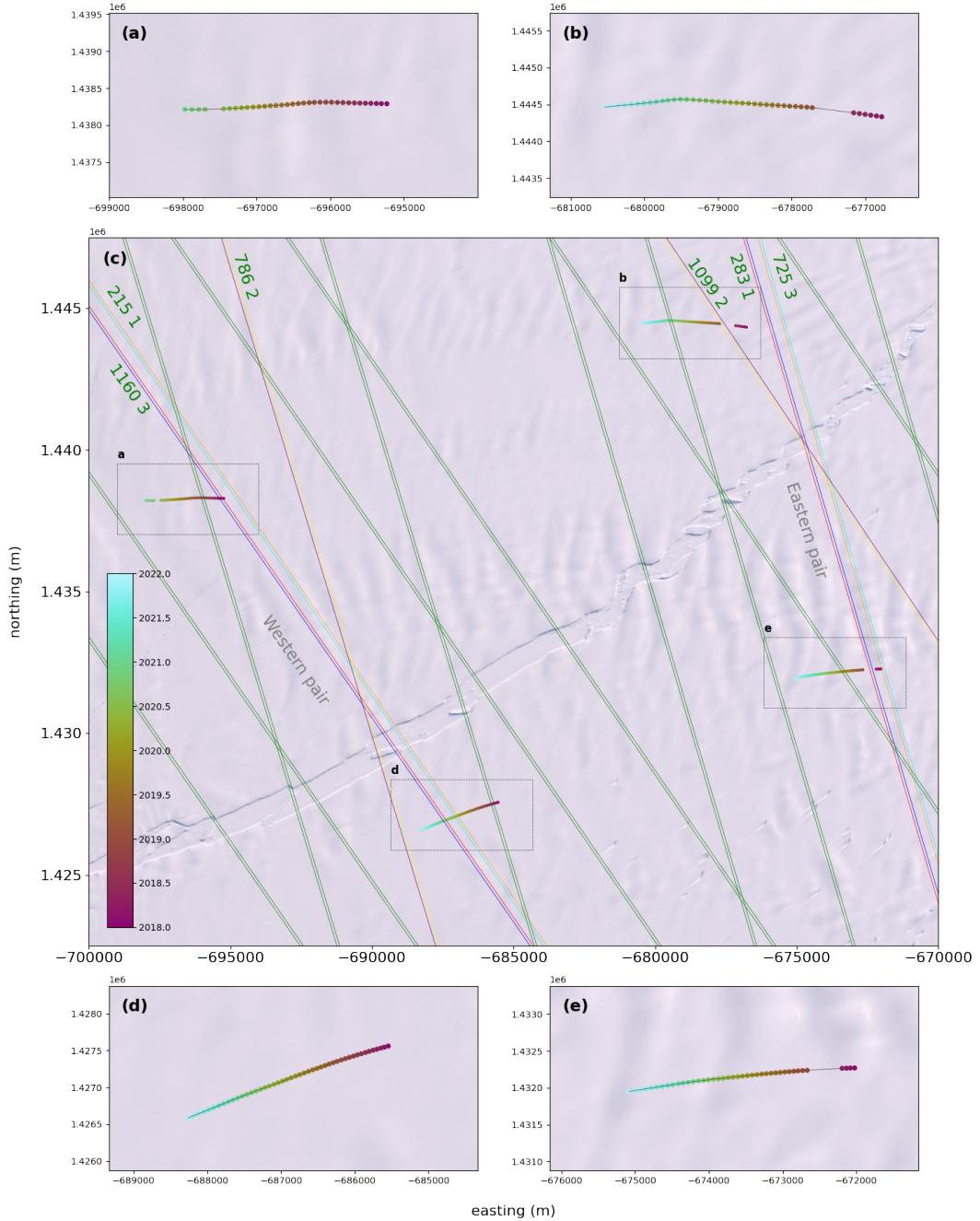
Figure 3. Movement of the GNSS receivers with ice flow. The six RGT beam pairs (RGT 215 1LR, RGT 1160 3LR, RGT 786 2LR, RGT 283 1LR, RGT 725 3LR, RGT 1099 2LR) used for comparison with rift-perpendicular opening rates between pairs of GNSS receivers are shown, colors correspond to Figs. 1, 4, 5 and 6.
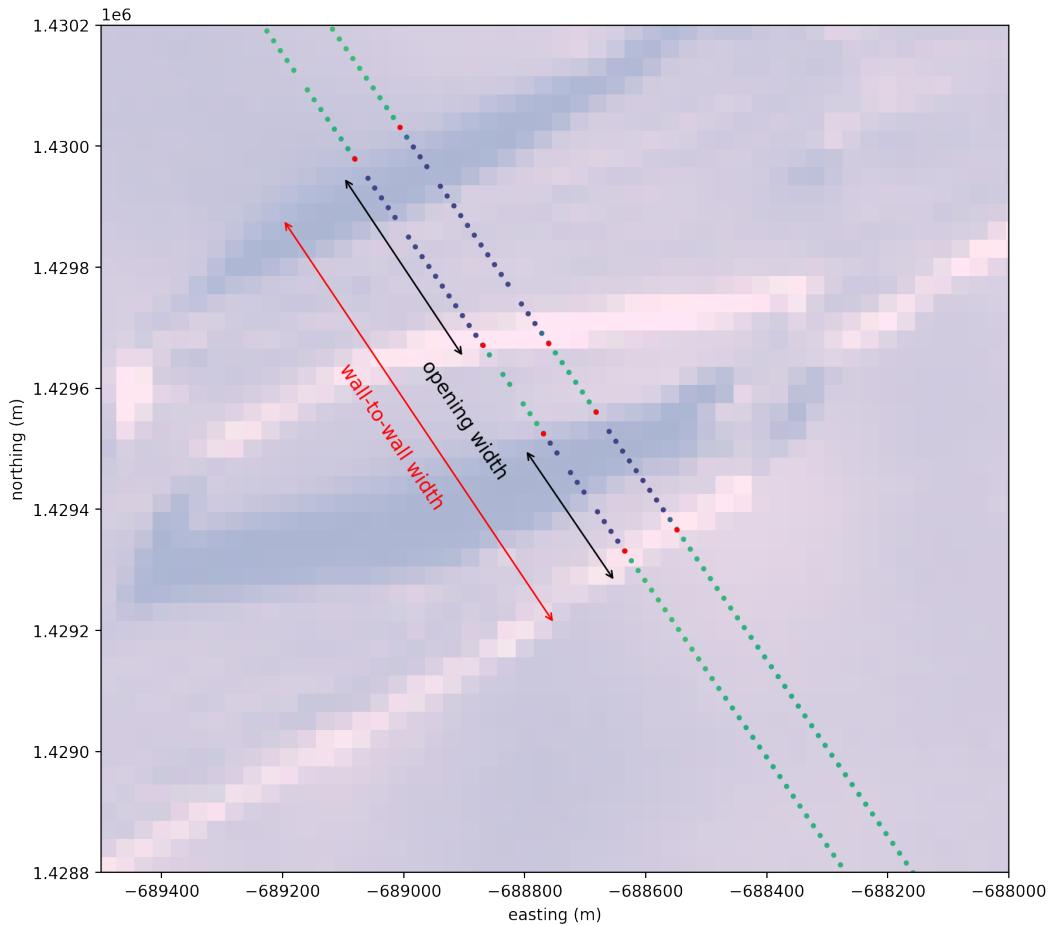
Figure 4. Rift "opening width" (the distance the rift has opened, ignoring the iceberg within the rift) and "wall-to-wall width" (the total distance between the seaward and landward rift walls) on a Landsat-8 image from 2019-04-12.
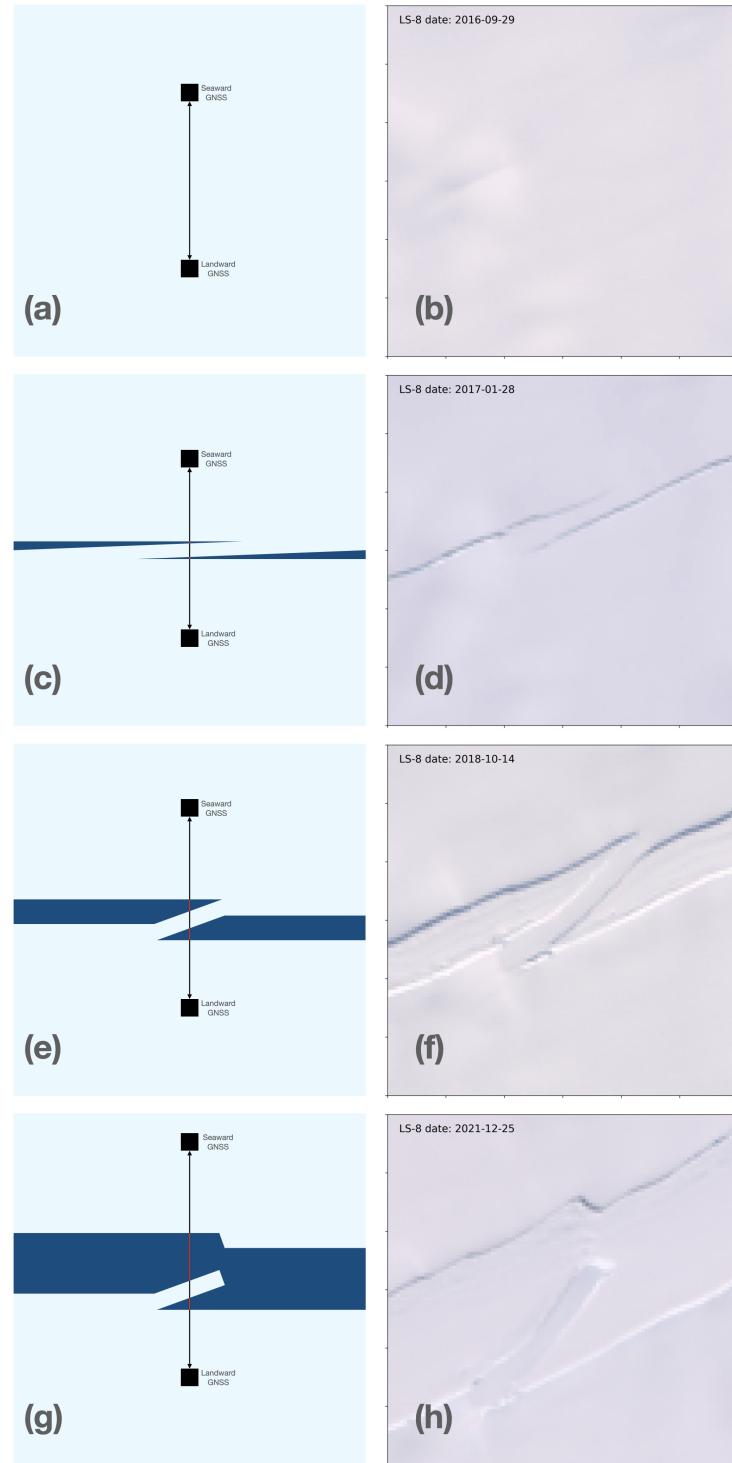
Figure 5. Schematic demonstrating why "opening width" (red) is the appropriate width to use when comparing widths from ICESat-2 and satellite imagery with GNSS receiver separation.
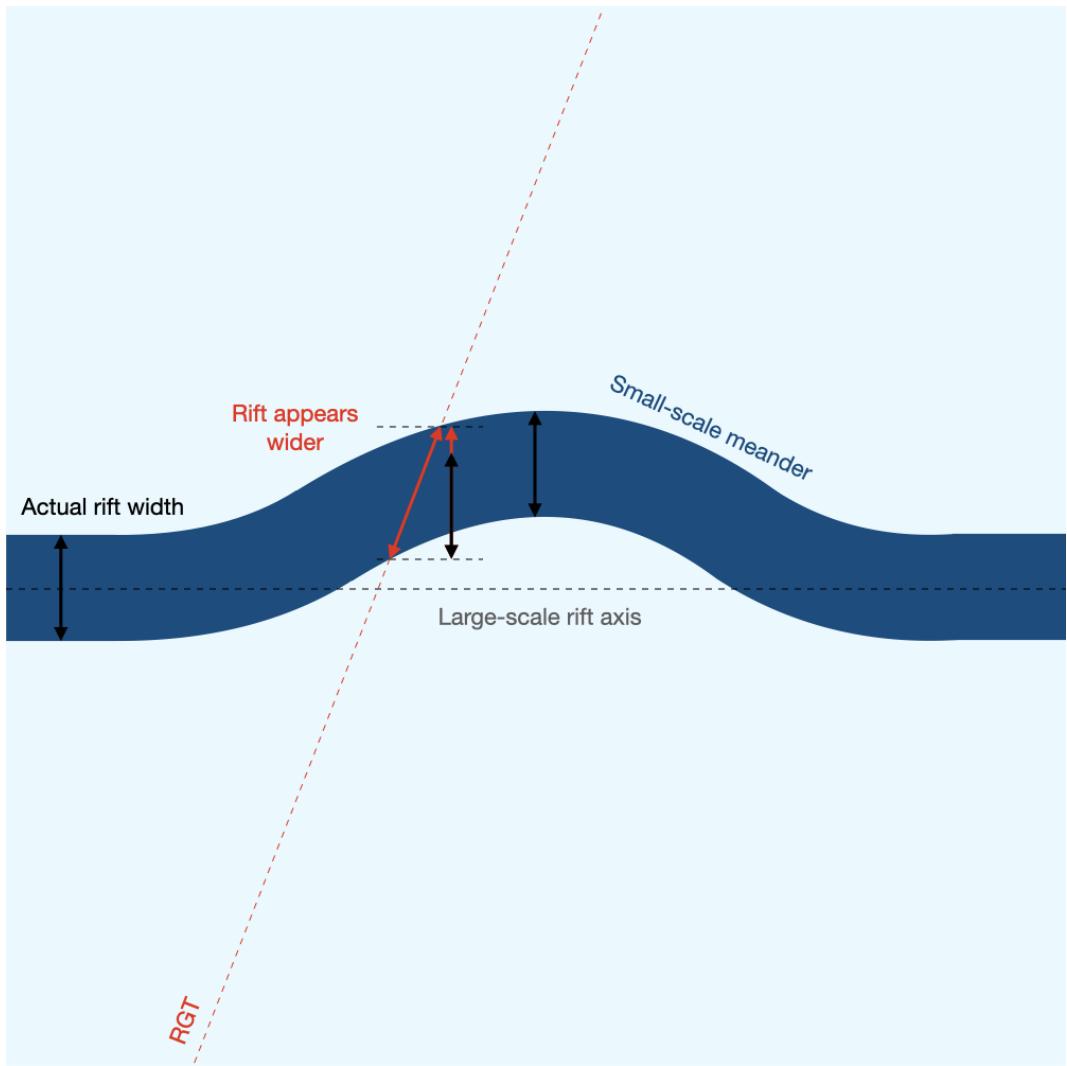
Figure 6. Schematic demonstrating the effect of small-scale meanders, caused by rift propagation between meteoric ice blocks (De Rydt et al., 2018; King et al., 2018), on rift width measurement. This is the situation for HC between the eastern pair of GNSS receivers, and may account for the occasional overestimation of rift width in Fig. 5. Red arrows show the measured rift width along the RGT and component perpendicular to the large-scale rift axis, compared to the actual rift width (black arrows).
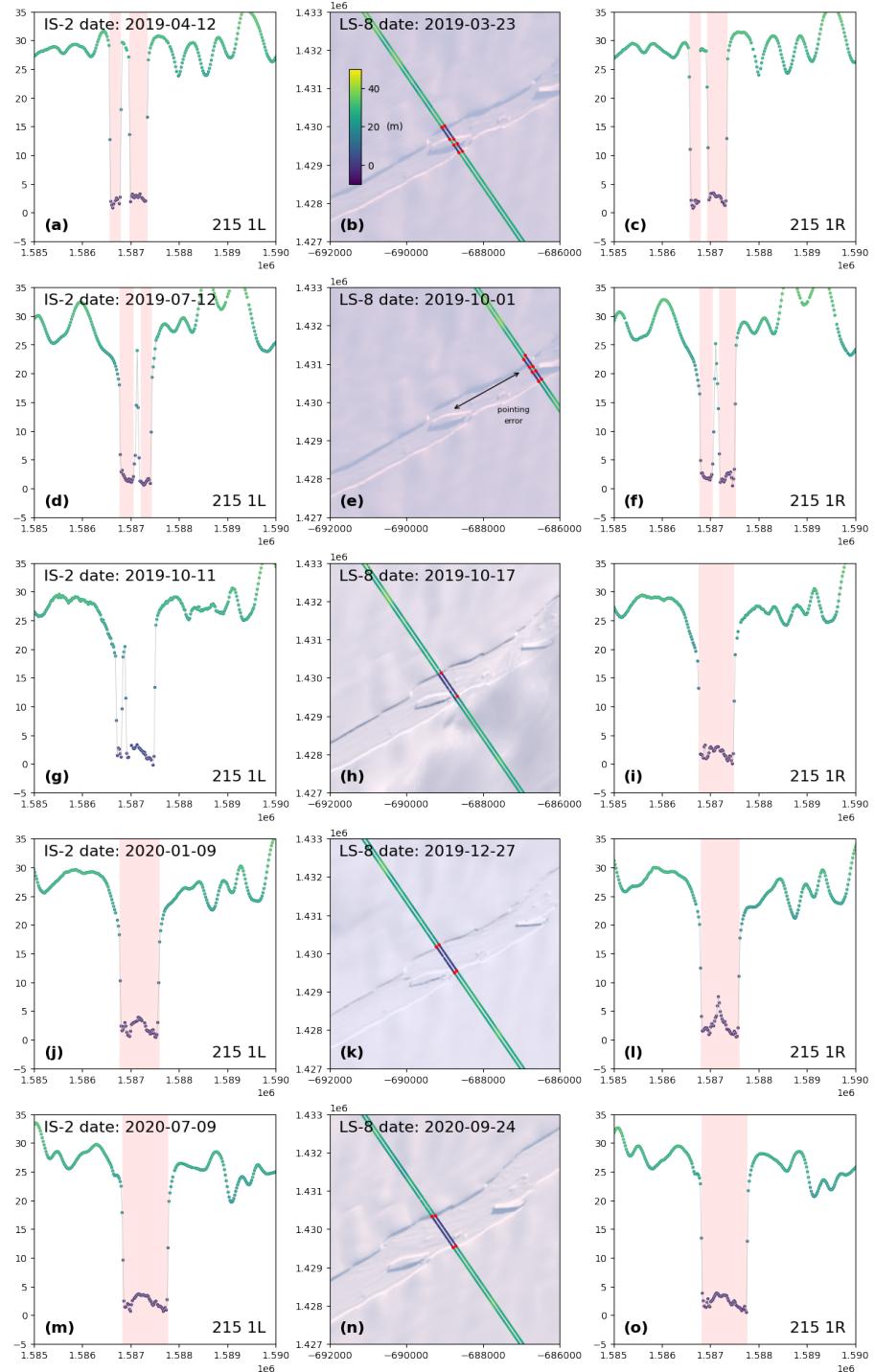
Figure 7. Example detections used in Fig. 4d and f along RGT 215 1LR. High confidence rift measurements are shown in light red. Note the satellite pointing error on 2019-07-12.
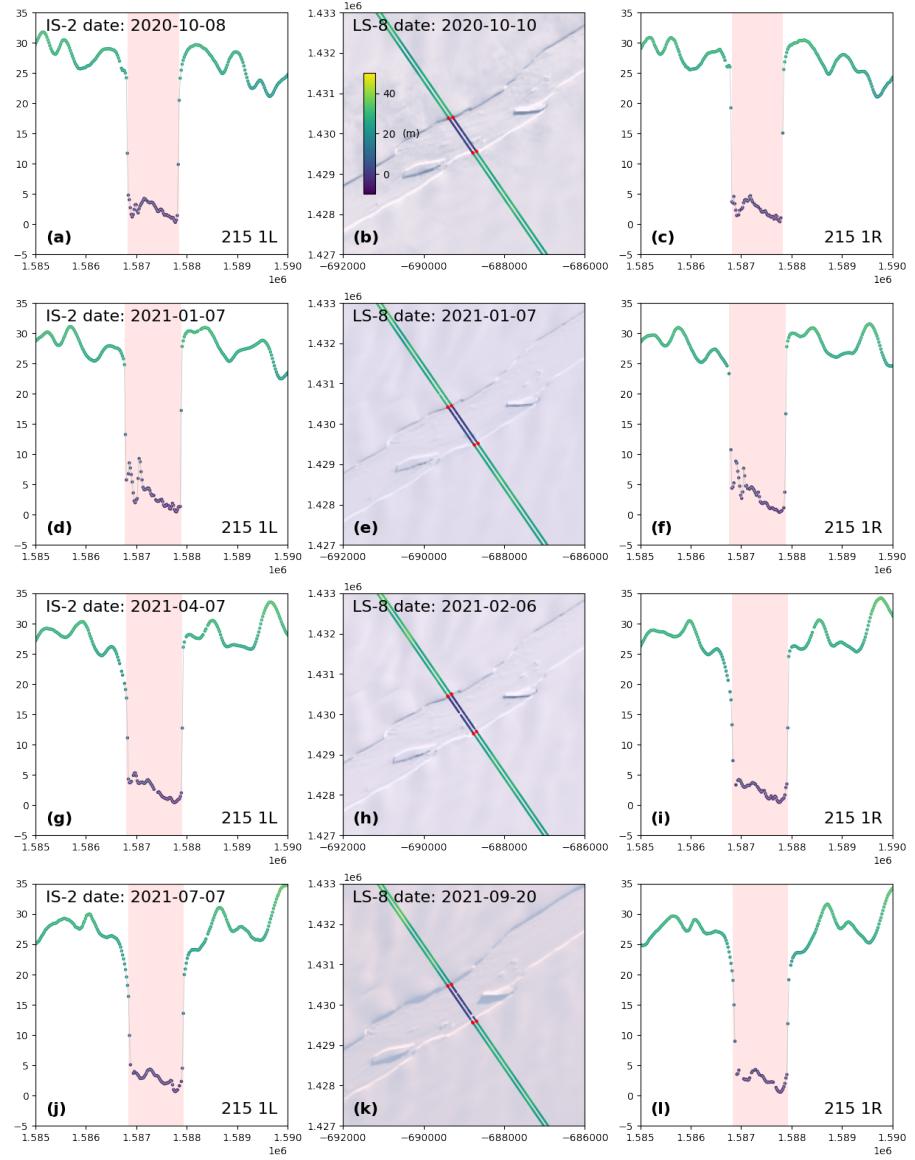
Figure 8. Example detections used in Fig. 4d and f along RGT 215 1LR (continued). High confidence rift measurements are shown in light red.
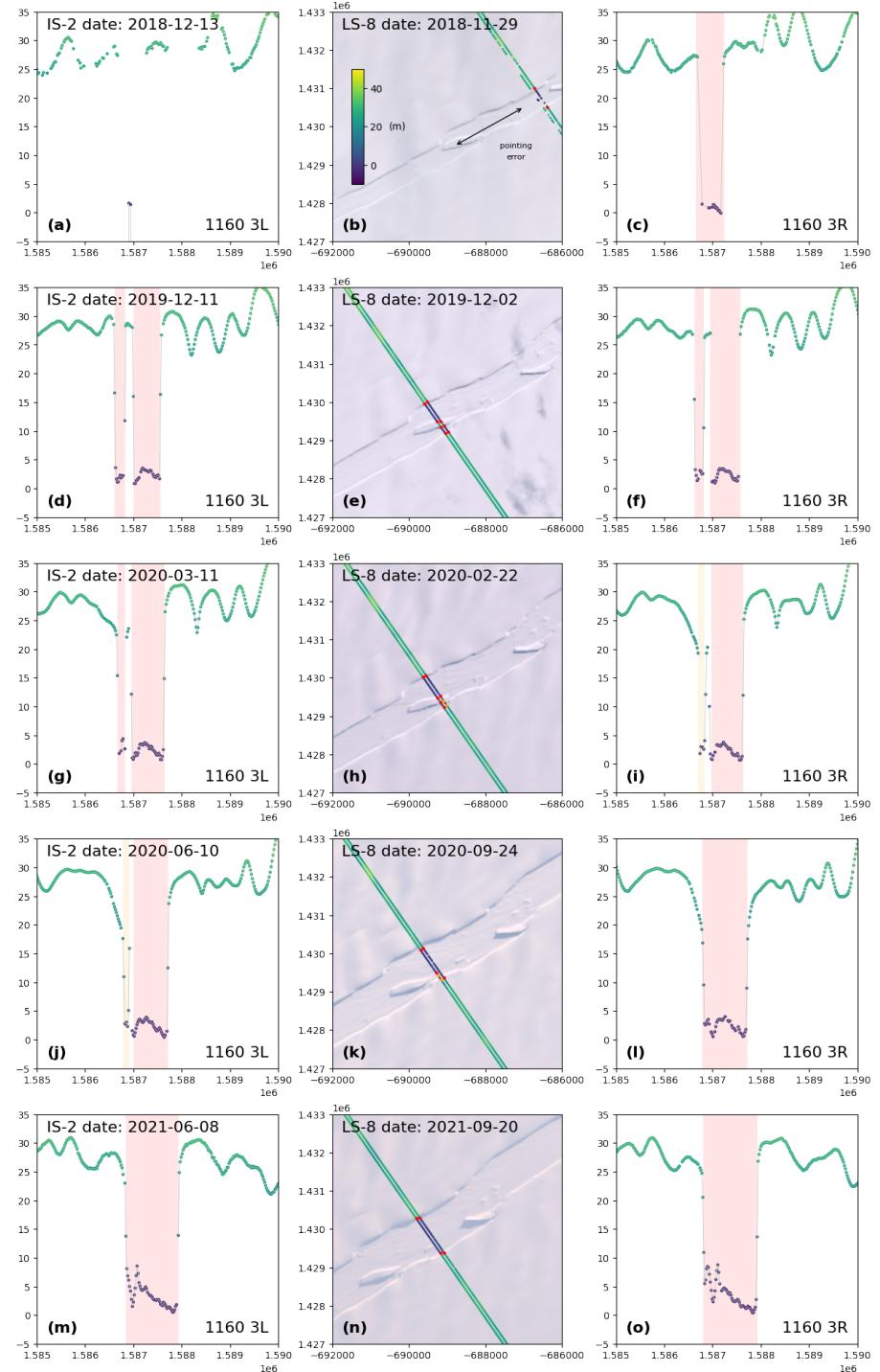
Figure 9. Example detections used in Fig. 4a and c along RGT 1160 3LR. High confidence rift measurements are shown in light red, lower confidence measurements in light orange. Note the ICESat-2 pointing error on 2018-12-13.
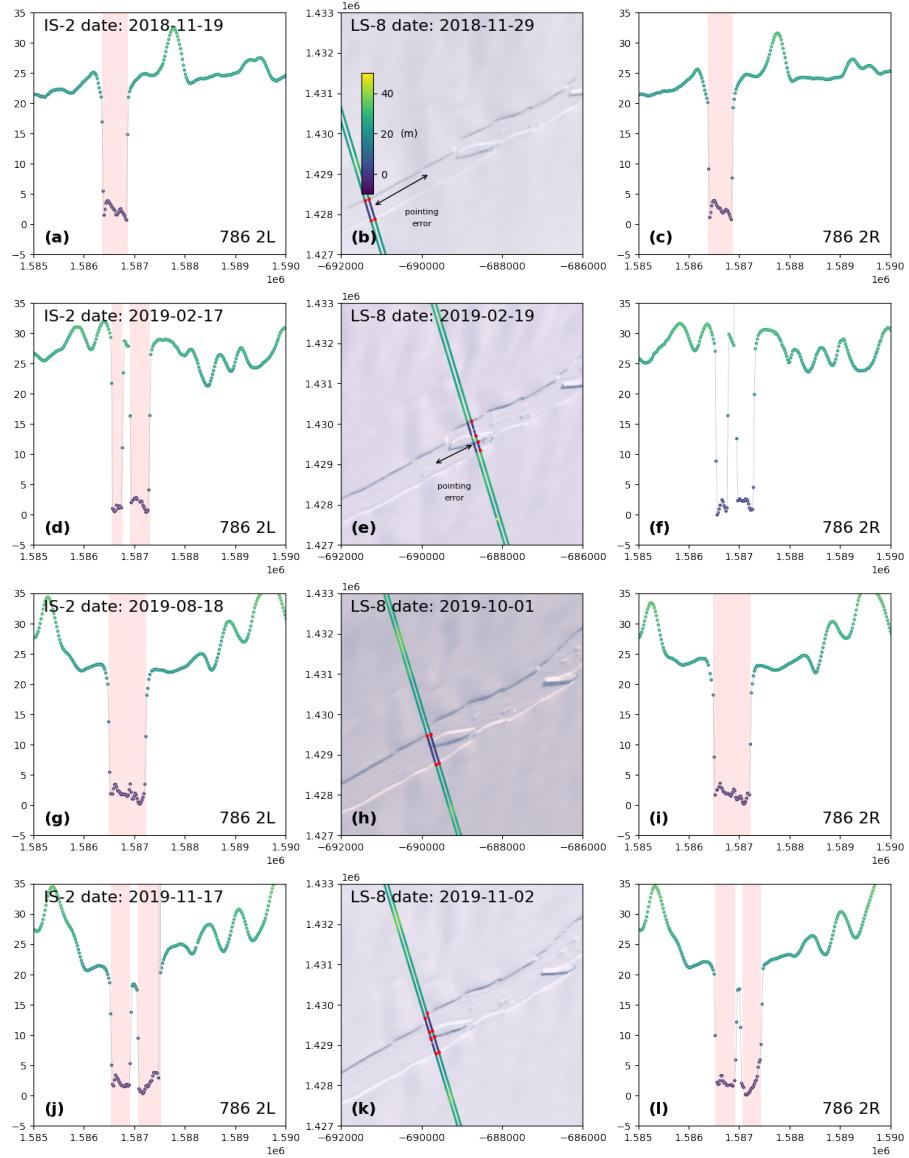
Figure 10. Example detections used in Fig. 4g and i along RGT 786 2LR. High confidence rift measurements are shown in light red. Note the ICESat-2 pointing errors on 2018-11-19 and 2019-02-17.
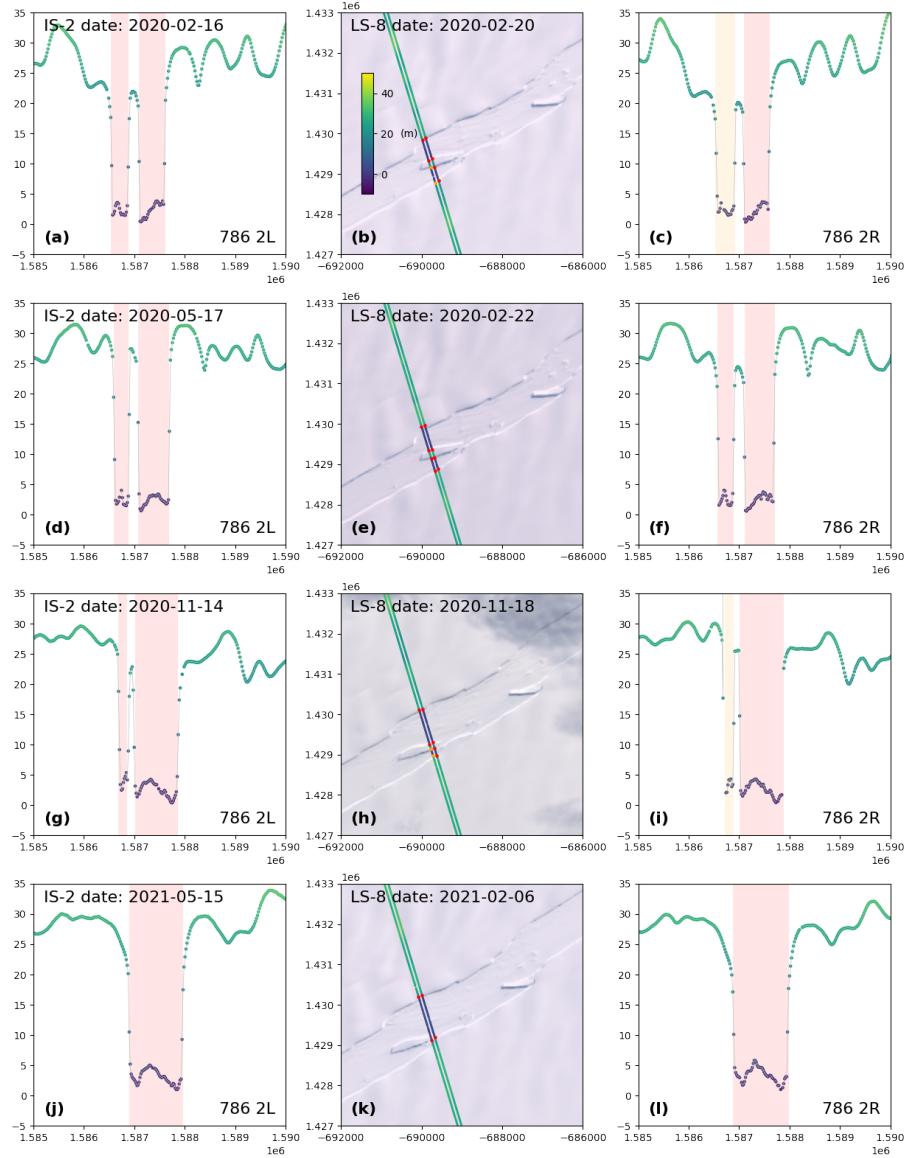
Figure 11. Example detections used in Fig. 4g and i along RGT 786 2LR (continued). High confidence rift measurements are shown in light red, lower confidence measurements in light orange.
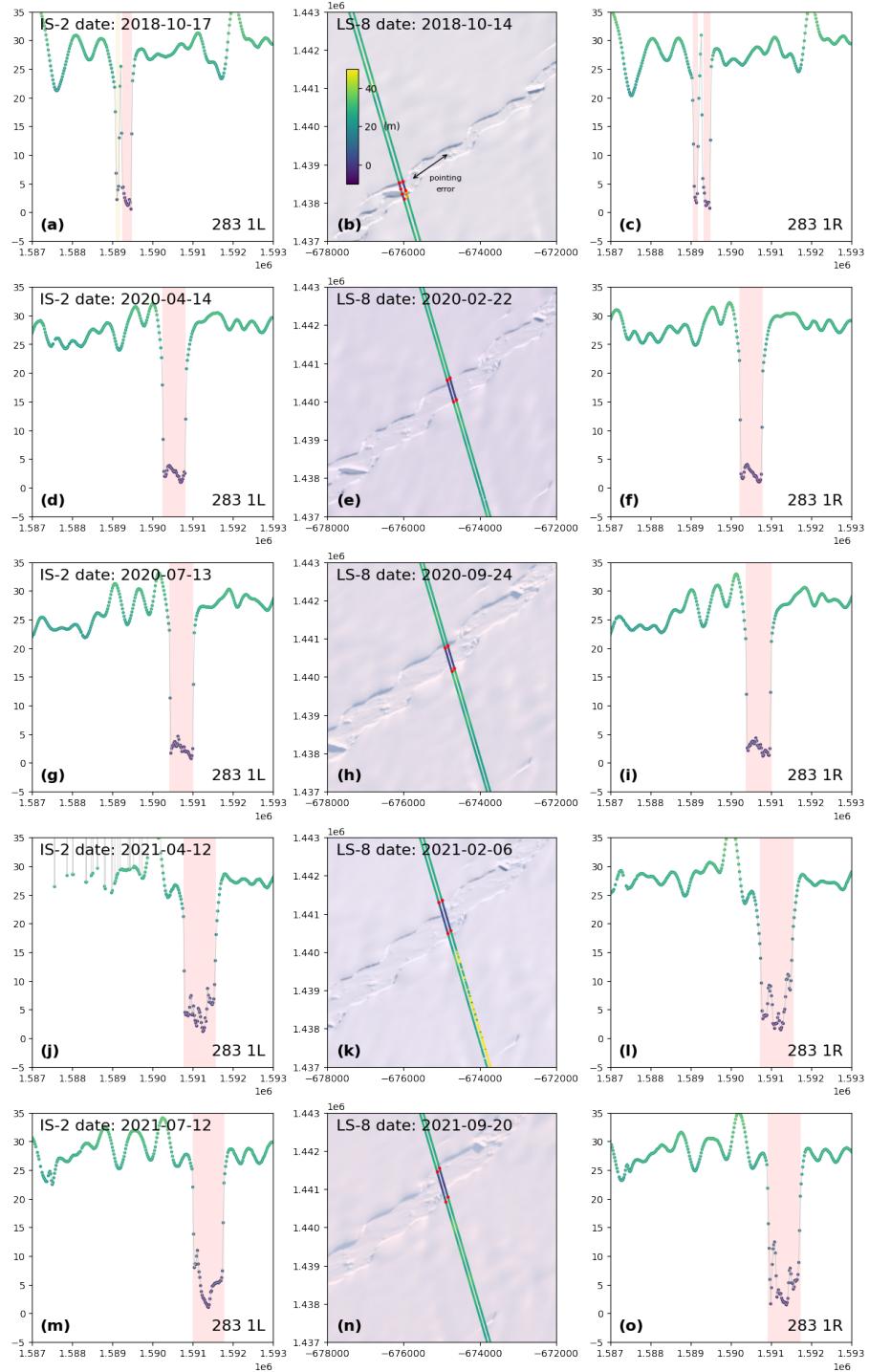
Figure 12. Example detections used in Fig. 5a and c along RGT 283 1LR. High confidence rift measurements are shown in light red, lower confidence measurements in light orange. Note the ICESat-2 pointing error on 2018-10-17.

.
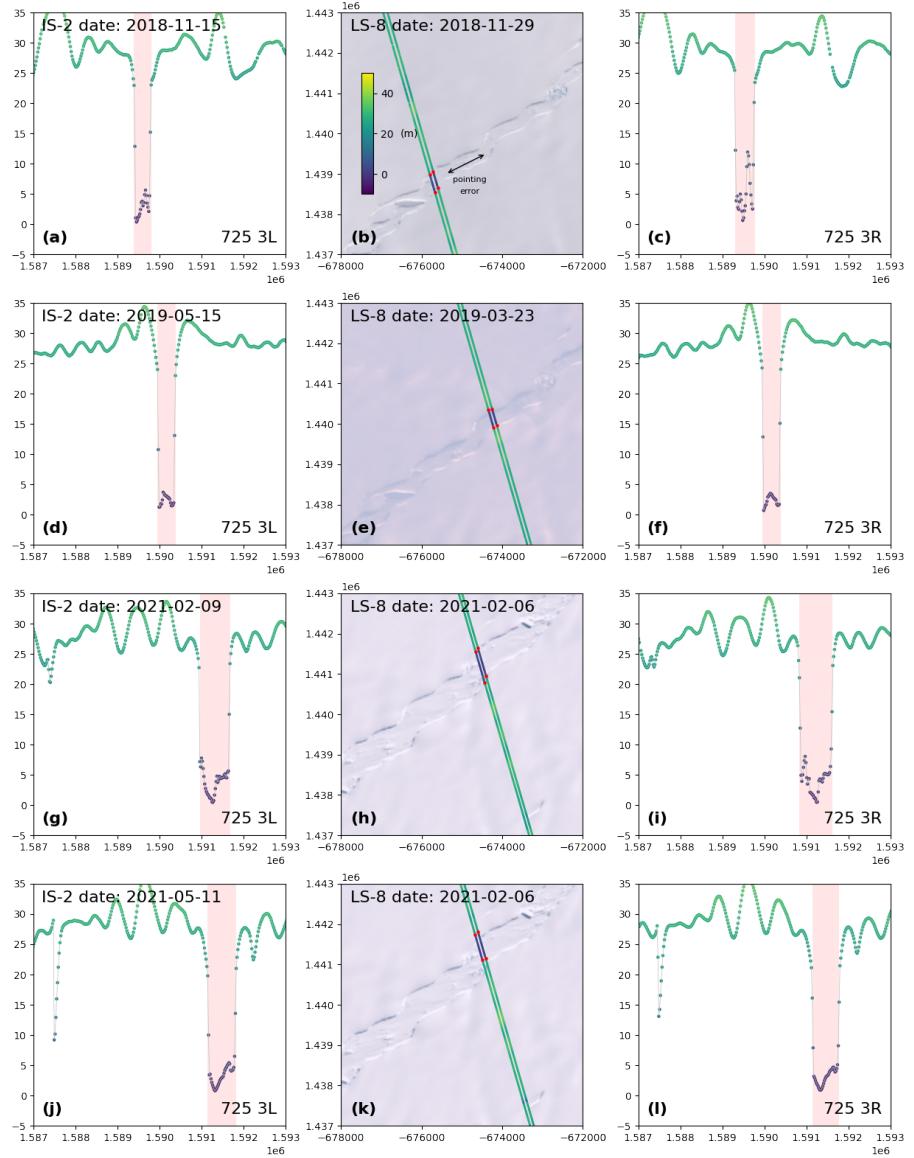
Figure 13. Example detections used in Fig. 5d and f along RGT 725 3LR. High confidence rift measurements are shown in light red. Note the ICESat-2 pointing error on 2018-11-15.
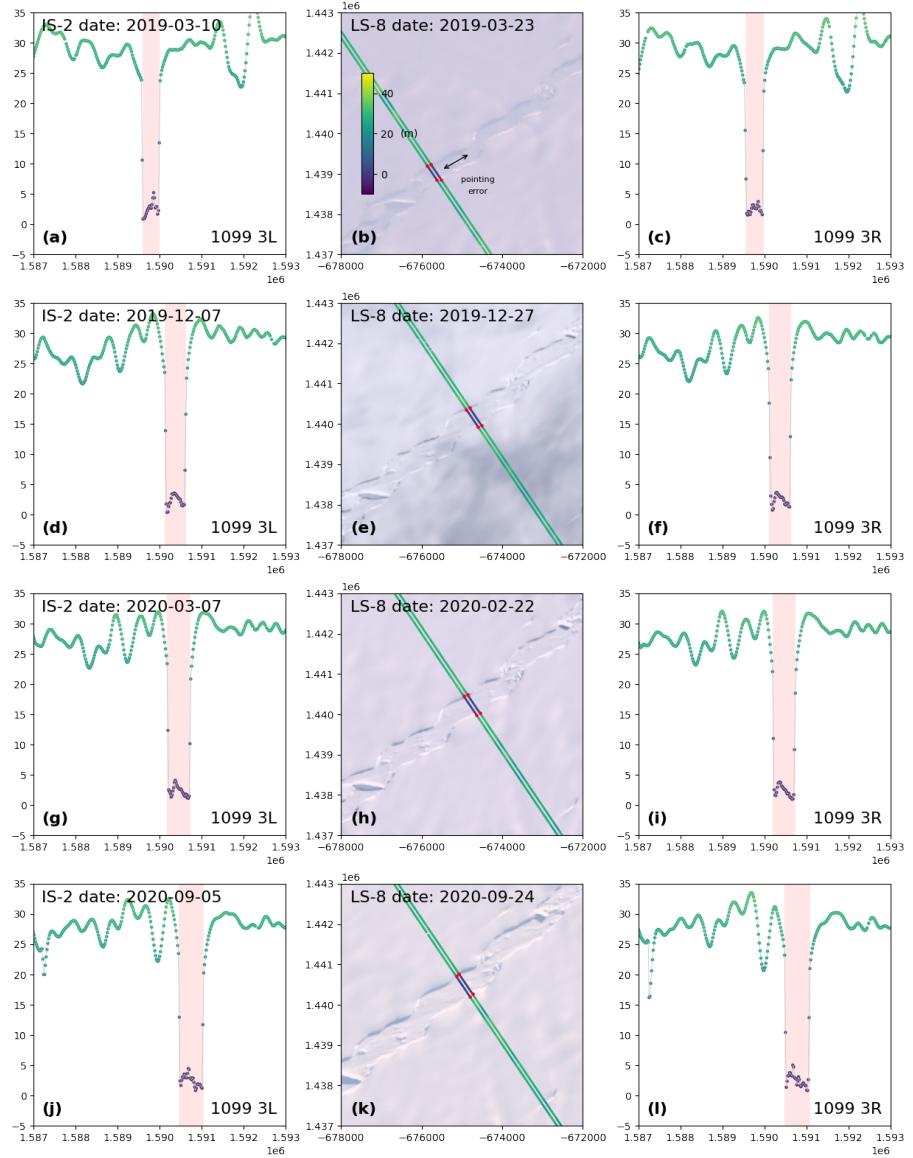
Figure 14. Example detections used in Fig. 5g and i along RGT 1099 2LR. High confidence rift measurements are shown in light red. Note the ICESat-2 pointing error on 2019-03-10.
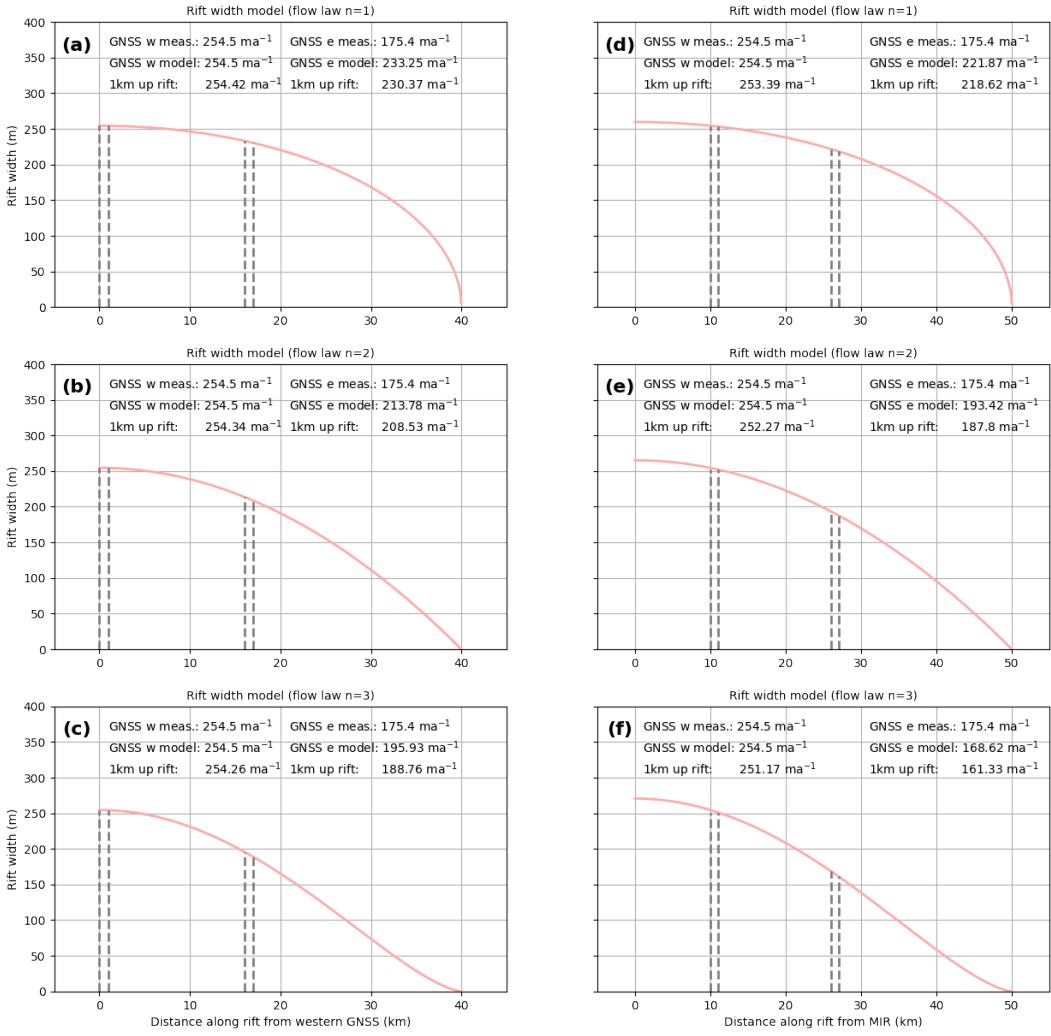
Figure 15. The effect of Lagrangian (GNSS) and Eulerian (ICESat-2 and satellite imagery) frames of reference on ICESat-2 rift measurement algorithm validation, resulting from the $\sim$700–1000 m a^{-1} flow of HC approximately perpendicular to ICESat-2 RGTs. Modeled HC opening rates (m a^{-1}) with different flow law parameters (n) assuming (**a**–**c**) that maximum opening occurs between the western GNSS pair or (**d**–**f**) that maximum opening occurs near MIR (50 km from the eastern rift tip). Dashed lines at 0 km and 1 km along rift in a–c and 10 km and 11 km along rift in d–f show the approximate locations of the western GNSS pair and a point 1 km upstream. Dashed lines at 16 km and 17 km along rift in a–c and 26 km and 27 km along rift in d–f show the corresponding approximate locations of the eastern GNSS and a point 1 km upstream. GNSS w/e meas. shows the divergence corrected opening rates from Fig. 6. GNSS w/e model shows the modeled opening rate at the GNSS locations (maximum opening values in d–f were modified until the modeled opening rate at the western GNSS pair agreed with observations). 1 km up rift shows the modeled opening rate 1 km upstream of the GNSS pair locations. In all instances, the difference between modeled and 1 km upstream opening rates is less than 10 m a^{-1}, and larger for the eastern GNSS pair, which is closer to the rift tip.
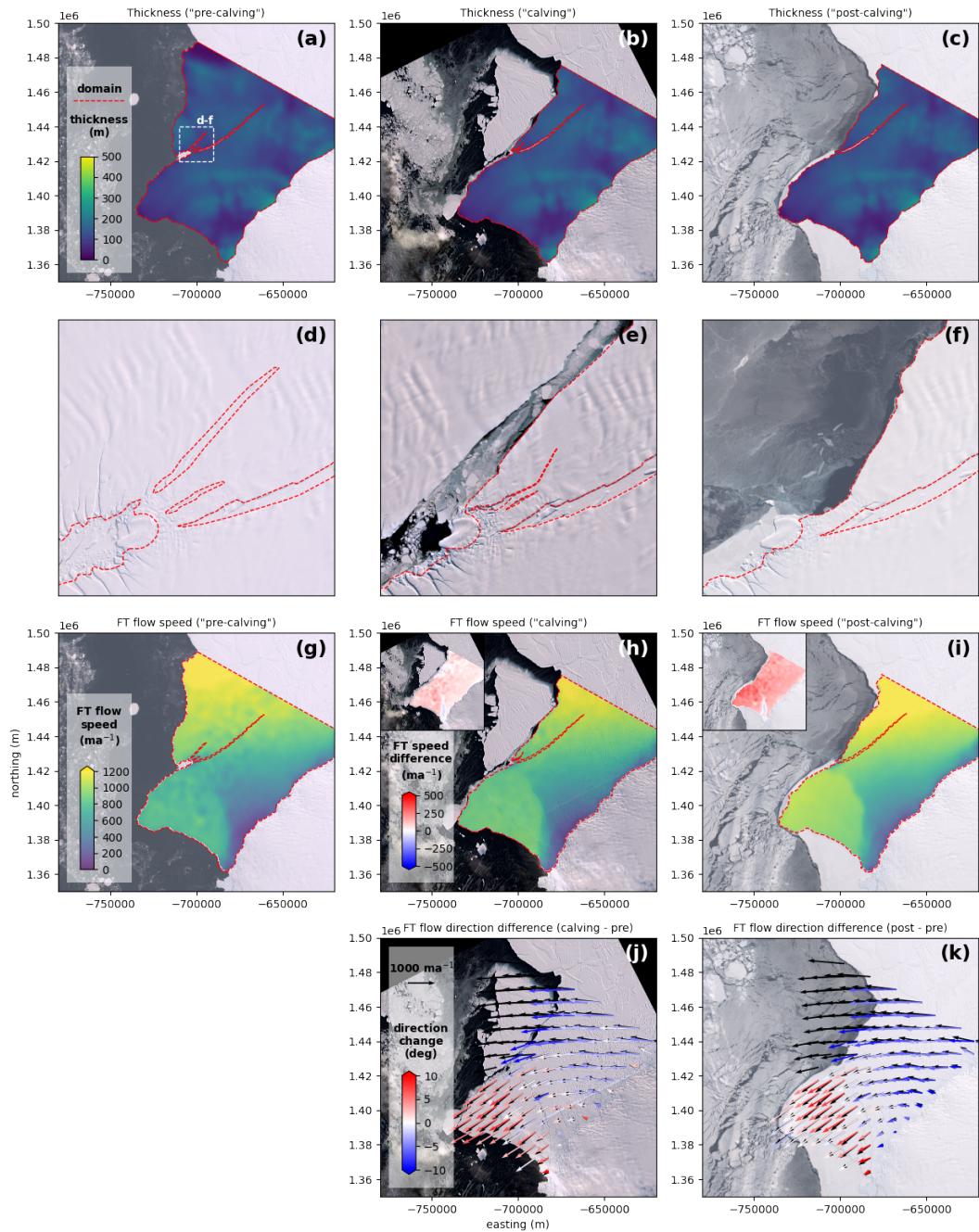
Figure 16. *icepack* model inputs. (**a–c**) Ice shelf thickness DEM cropped to the "pre-calving", "calving" and "post-calving" domains (dashed red lines). Dashed white box in a show the location of d–f. (**d–f**) Fractures in the vicinity of McDonald Ice Rumples in the 3 domains. d includes the ∼13 km-long beginning of North Rift. (**g–i**) Ice flow speed from feature tracking of Sentinel-1 SAR scene pairs. Insets show ice flow speed change compared to prior to calving from NR, demonstrating an increase in ice flow speed. (**j, k**) Ice flow direction and magnitude change compared to prior to calving. Black arrows show "pre-calving" velocity, colored arrows show "calving" (j) and "post-calving" (k) velocity, highlighting acceleration and angular change in flow direction (red shows clockwise redirection of flow, blue shows anti-clockwise redirection of flow).
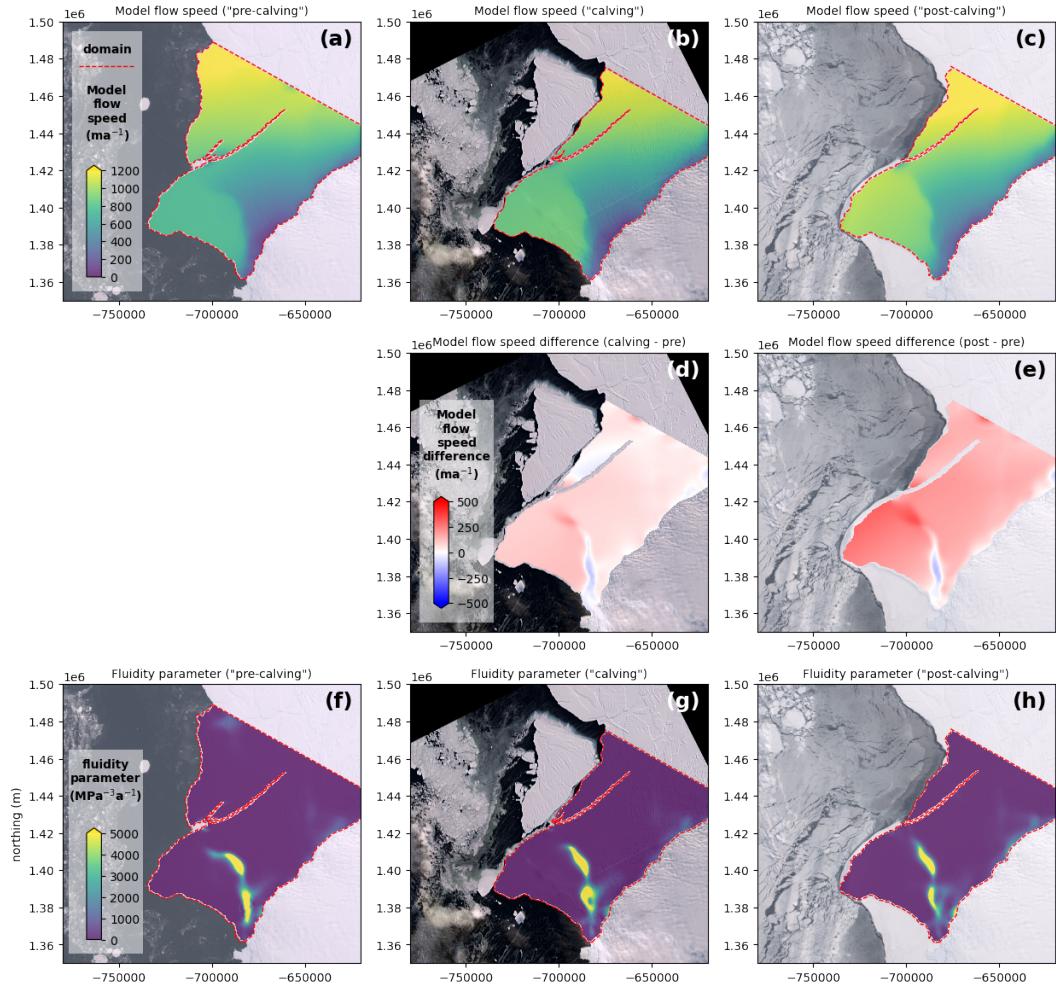
Figure 17. *icepack* model outputs. (**a**–**c**) Modeled ice flow speed. (**d**, **e**) Modeled ice flow speed change compared to prior to calving from NR. (**f**–**h**) Modeled fluidity parameter.
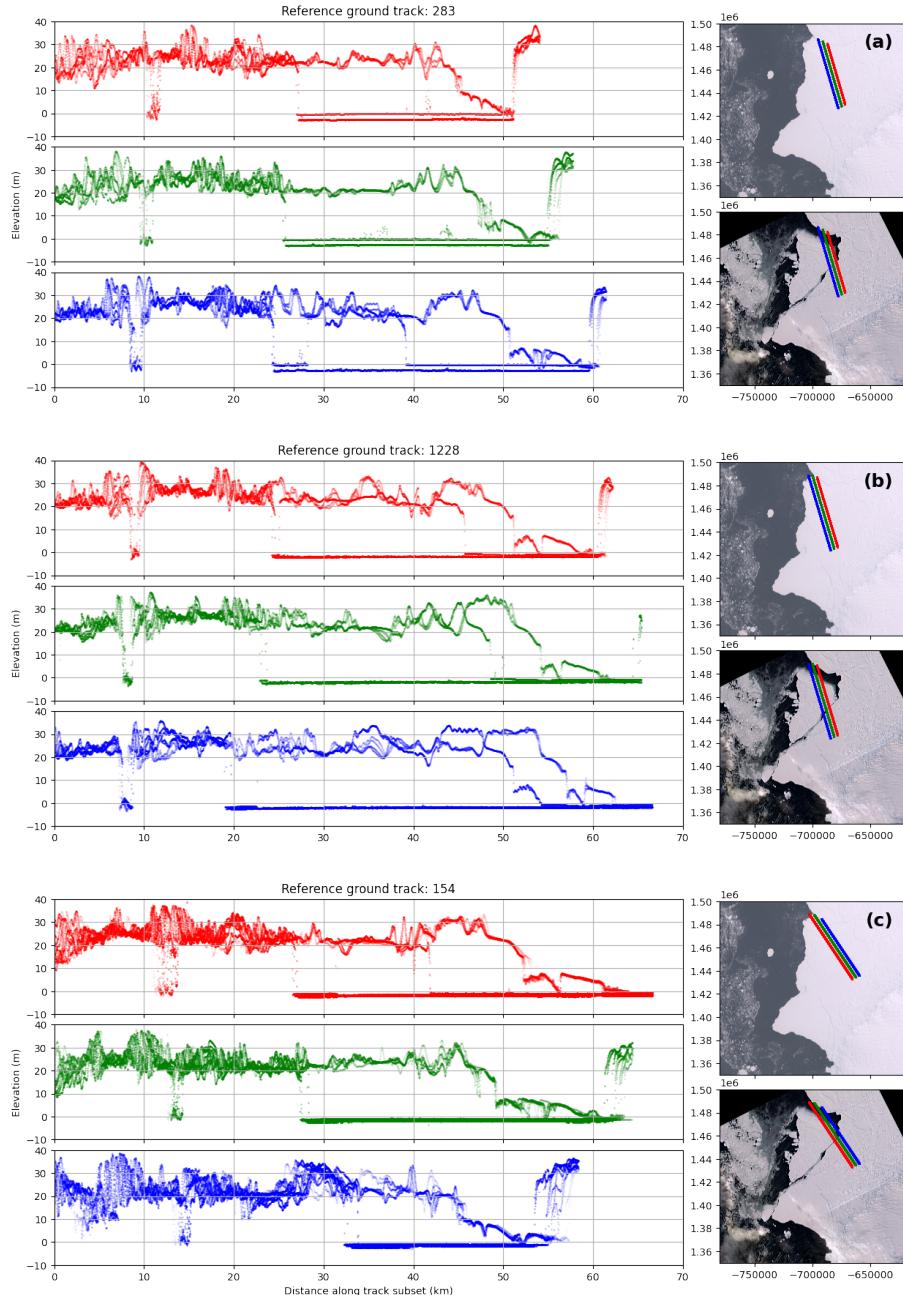
Figure 18. Cycle 5 to 15 SlideRule ICESat-2 elevations along RGTs which cross the calving fronts before and after calving from NR, for (**a**) RGT 283 (**b**) RGT 1228 (**c**) RGT 154. Red, green and blue denote different beam pairs, with strong and weak beams within each pair combined. Cycles are denoted by different color intensity, with intensity increasing with time.
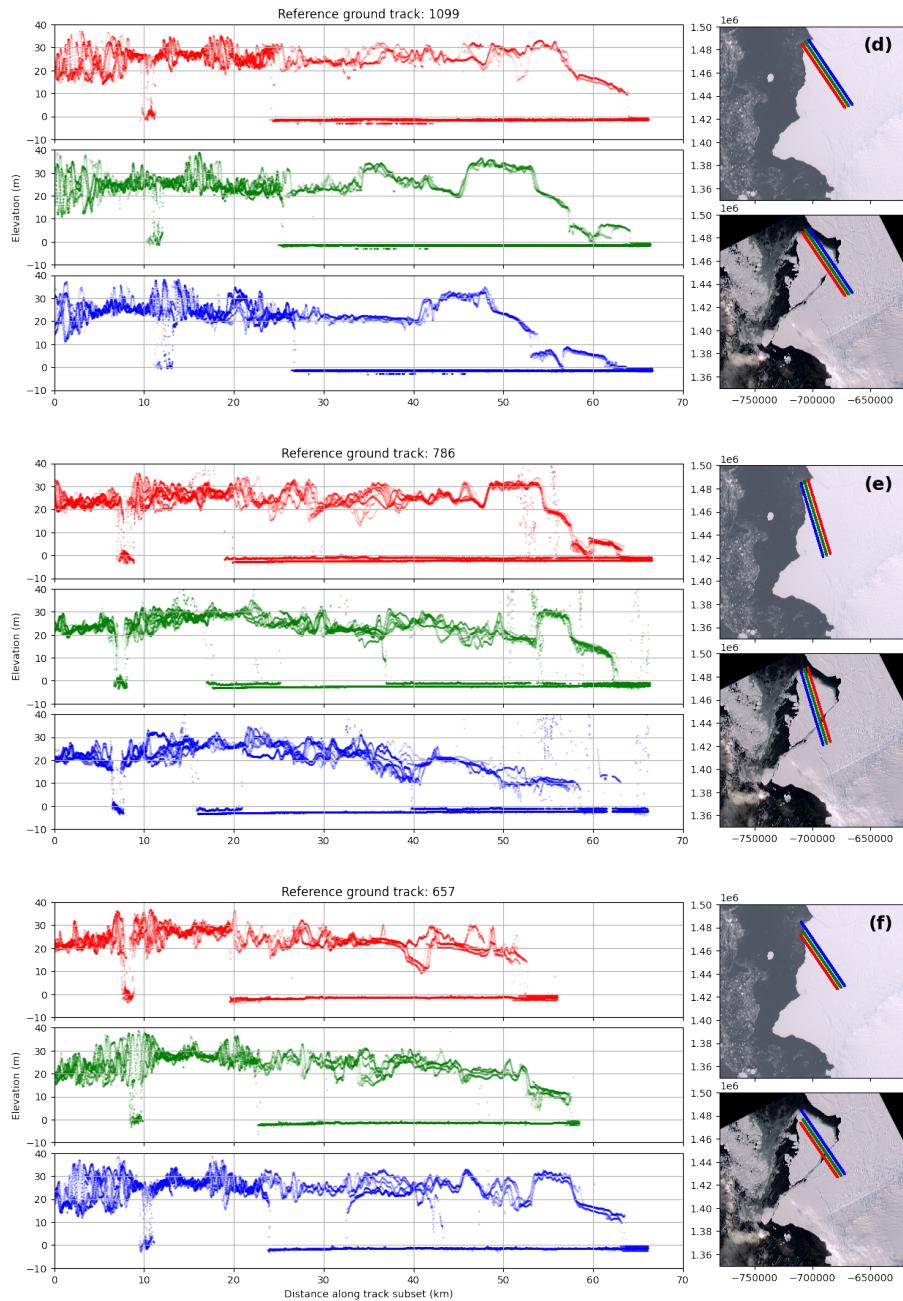
Figure 19. As Fig. S18 for (**d**) RGT 1099 (**e**) RGT 786 (**f**) RGT 657.
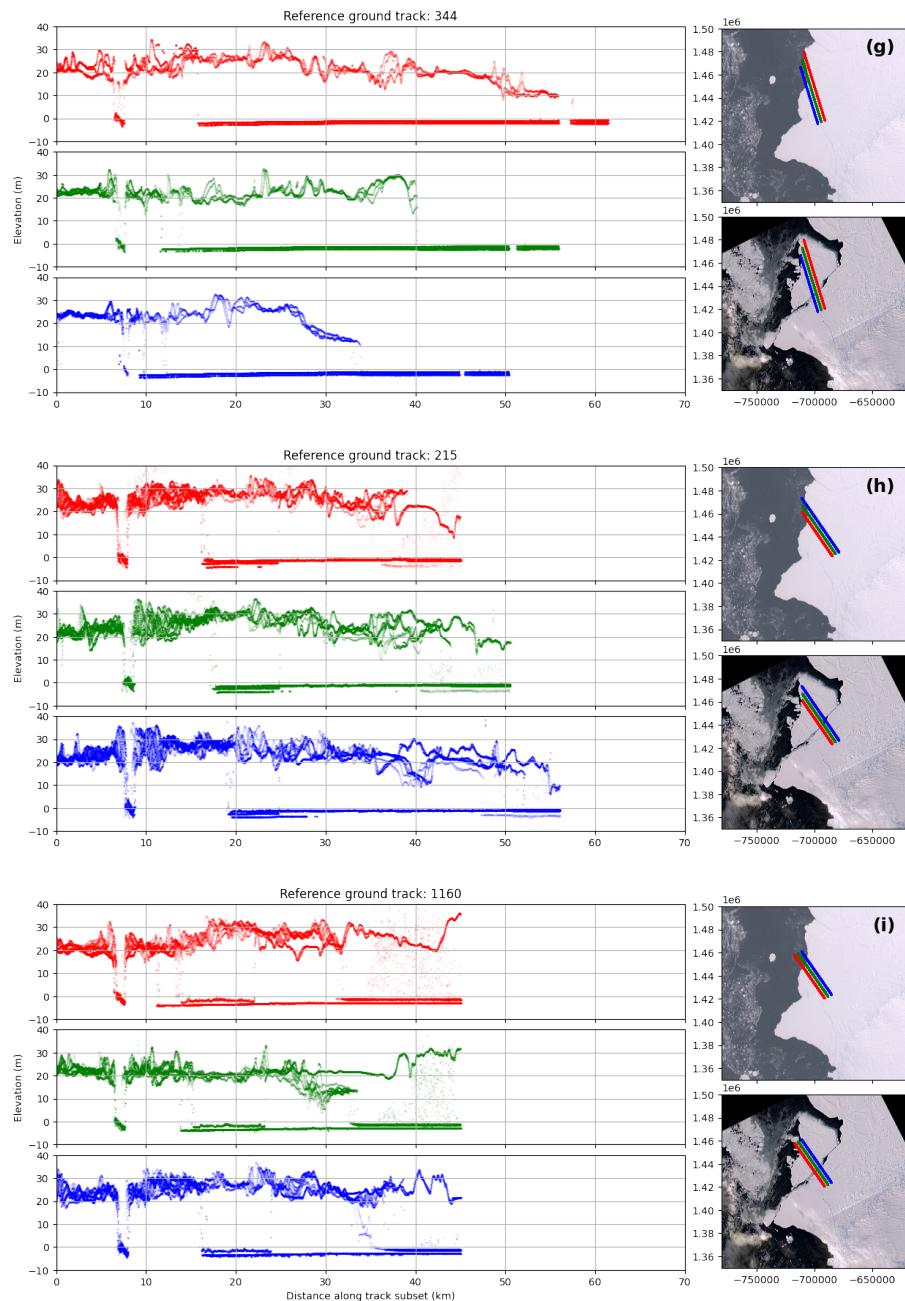
Figure 20. As Fig. S18 for (**g**) RGT 344 (**h**) RGT 215 (**i**) RGT 1160 .
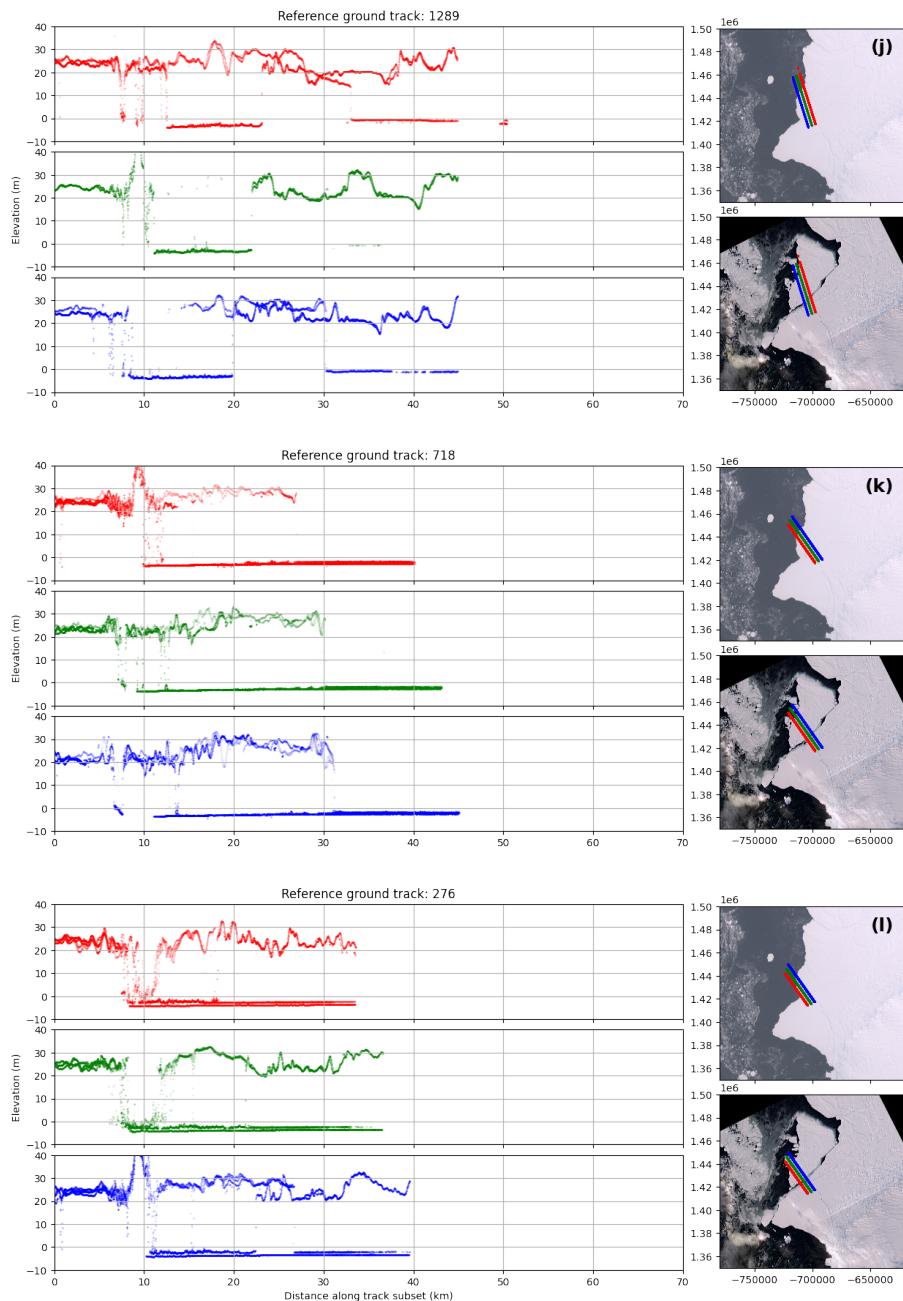
Figure 21. As Fig. S18 for (**j**) RGT 1289 (**k**) RGT 718 (**l**) RGT 276.

Table 1. WorldView-1-3 satellite images used for Halloween Crack width digitization along RGT 215 1LR, RGT 1160 3LR and RGT 786 2LR between the western pair of GNSS receivers.

Platform	Date	ID
WorldView-1	2016-12-04	WV01_20161204052108_10200100599B5200
WorldView-3	2016-12-11	WV03_20161211020616_1040010026561300
WorldView-1	2017-11-17	WV01_20171117134024_1020010068224000
WorldView-1	2017-11-22	WV01_20171122132254_10200100693F3E00
WorldView-1	2018-03-13	WV01_20180313131607_1020010072B34B00
WorldView-2	2018-12-04	WV02_20181204034234_10300100890D9800
WorldView-1	2019-04-11	WV01_20190411123307_102001007D73A200
WorldView-3	2019-09-18	WV03_20190918110239_10400100519B7300
WorldView-1	2019-11-02	WV01_20191102135533_1020010092CB5600
WorldView-1	2019-12-02	WV01_20191202135059_102001008F659100
WorldView-3	2020-02-15	WV03_20200215104103_1040010058701900
WorldView-1	2020-03-22	WV01_20200322134650_102001009325B500
WorldView-3	2020-03-24	WV03_20200324104234_104001005BCA7B00
WorldView-1	2020-11-29	WV01_20201129054413_102001009EA34400
WorldView-2	2020-12-07	WV02_20201207094927_10300100AE896000
WorldView-3	2020-12-09	WV03_20201209104515_104001006329D800
WorldView-1	2021-01-19	WV01_20210119054306_10200100A2246D00
WorldView-1	2021-01-19	WV01_20210119054212_10200100A22D6900
WorldView-3	2022-01-03	WV03_20220103020527_1040010072CE8500
WorldView-2	2022-01-07	WV02_20220107032223_10300100CB76C500

Table 2. WorldView-1-3 satellite images used for Halloween Crack width digitization along RGT 283 1LR, RGT 725 3LR and RGT 1099 2LR between the eastern pair of GNSS receivers.

Platform	Date	ID
WorldView-1	2017-04-02	WV01_20170402131921_1020010061410900
WorldView-1	2017-11-17	WV01_20171117134024_1020010068224000
WorldView-1	2017-11-21	WV01_20171121134611_102001006B664400
WorldView-3	2019-01-08	WV03_20190108024204_1040010045D59A00
WorldView-1	2019-04-12	WV01_20190412134450_1020010086A5AA00
WorldView-2	2019-09-17	WV02_20190917105429_1030010099561200
WorldView-1	2019-11-02	WV01_20191102135533_1020010092CB5600
WorldView-1	2019-12-12	WV01_20191212053208_102001008EA0FE00
WorldView-1	2020-03-18	WV01_20200318134132_1020010097598D00
WorldView-1	2020-03-22	WV01_20200322134704_1020010097B0DB00
WorldView-3	2020-03-25	WV03_20200325105744_104001005980FD00
WorldView-1	2020-10-30	WV01_20201030054839_102001009CBC1C00
WorldView-1	2020-11-29	WV01_20201129054413_102001009EA34400
WorldView-1	2021-01-19	WV01_20210119054244_10200100A1C45600
WorldView-1	2021-09-07	WV01_20210907132654_10200100B6265D00
WorldView-1	2021-12-05	WV01_20211205054543_10200100BA8E5500
WorldView-2	2022-01-07	WV02_20220107032223_10300100CB76C500
WorldView-1	2022-02-15	WV01_20220215133306_10200100BF581B00

Table 3. Halloween Crack width digitization along RGT 215 1LR, RGT 1160 3LR and RGT 786 2LR between the western pair of GNSS receivers from WorldView-1-3, used in Fig. 4.

Platform	Date	width (m) - opening width (wall-to-wall width)					
		1160 3L	1160 3R	215 1L	215 1R	786 2L	786 2R
WV1	2016-12-04	16.7	16.8	21.8	14.0	16.5	16.8
WV3	2016-12-11	17.9	18.5	17.4	14.8	18.3	17.6
WV1	2017-11-17	224.7	219.6	230.0	228.8	211.7	214.1
WV1	2017-11-22	230.9	222.1	232.1	230.8	215.1	212.2
WV1	2018-03-13	318.8	319.4	318.1	321.0	303.8	301.6
WV2	2018-12-04	533.8 (591.8)	548.8	515.0 (715.6)	505.0 (730.4)	543.0	538.6
WV1	2019-04-11	612.7 (806.6)	617.8 (781.6)	619.0 (789.7)	628.0 (798.9)	645.8	649.6
WV3	2019-09-18	725.1 (908.8)	715.3 (916.1)	732.0 (769.5)	719.0 (843.6)	765.3	832.3 (872.7)
WV1	2019-11-02	768.6 (932.2)	760.7 (941.3)	750.3	806.2 (756.0)	869.7 (909.5)	801.9 (950.7)
WV1	2019-12-02	786.9 (946.1)	782.2 (954.0)	785.4	775.1	823.2 (968.4)	827.6 (987.9)
WV3	2020-02-15	853.4 (965.0)	865.8 (1003.1)	849.0	834.0	-	-
WV1	2020-03-22	869.7 (937.7)	882.9 (998.5)	880.0	872.4	888.3 (1097.2)	889.5 (1097.0)
WV3	2020-03-24	876.1 (937.7)	884.4 (1001.2)	878.0	874.0	893.2 (1102.8)	894.5 (1100.5)
WV1	2020-11-29	1070.7	1070.2	1118.3	1077.8	1108.4 (1220.2)	1094.5 (1195.2)
WV2	2020-12-07	1078.7	1077.0	1088.4	1116.9	1114.2 (1225.8)	1093.5 (1190.2)
WV3	2020-12-09	1081.7	1079.3	1120.3	1097.8	1115.8 (1227.5)	1098.4 (1191.6)
WV1	2021-01-19	1103.3	1090.6	1112.3	1124.4	1121.2 (1204.6)	1148.9
WV1	2021-01-19	1102.8	1088.6	1118.5	1129.8	-	-
WV3	2022-01-03	1141.8	1165.6	1123.8	1109.0	1172.0	1206.7
WV2	2022-01-07	1146.9	1163.2	1126.4	1119.0	-	-

Table 4. Halloween Crack width digitization along RGT 283 1LR, RGT 725 3LR and RGT 1099 2LR between the eastern pair of GNSS receivers from WorldView-1-3, used in Fig. 5.

Platform	Date	width (m) - opening width					
		283 1L	283 1R	725 3L	725 3R	1099 2L	1099 2R
WV1	2017-04-02	43.5	41.7	36.3	39.3	36.0	39.3
WV1	2017-11-17	142.6	148.2	198.0	155.8	191.9	143.1
WV1	2017-11-21	139.5	154.2	191.1	155.9	191.9	162.2
WV3	2019-01-08	412.3	429.8	363.3	256.5	335.5	320.7
WV1	2019-04-12	489.1	466.6	385.9	400.7	394.6	415.3
WV2	2019-09-17	460.9	448.3	450.5	482.5	463.1	456.6
WV1	2019-11-02	467.8	474.2	511.4	-	474.2	487.4
WV1	2019-12-12	489.2	482.6	519.2	526.3	504.9	487.2
WV1	2020-03-18	534.8	561.3	545.7	523.0	532.1	532.4
WV1	2020-03-22	539.3	560.5	531.7	512.8	531.5	534.4
WV3	2020-03-25	-	-	535.5	513.5	-	-
WV1	2020-10-30	620.6	619.5	780.0	774.6	639.1	616.7
WV1	2020-11-29	631.9	624.9	790.9	788.9	665.4	643.6
WV1	2021-01-19	652.4	707.2	810.0	777.4	685.9	679.5
WV1	2021-09-07	682.8	694.0	640.3	647.7	703.1	715.9
WV1	2021-12-05	-	-	662.4	663.1	-	-
WV2	2022-01-07	691.7	668.5	672.0	671.2	620.9	609.5
WV1	2022-02-15	677.2	682.9	672.2	673.3	654.4	625.9

Table 5. Landsat-8 OLI and Landsat-9 OLI-2 satellite images used for Halloween Crack width digitization. Imagery downloaded from https://earthexplorer.usgs.gov. Landsat Images courtesy of U.S. Geological Survey.

Platform	Date	ID
Landsat-8	2017-11-12	LC08_L1GT_182114_20171112_20201016_02_T2
Landsat-8	2017-12-21	LC08_L1GT_183114_20171221_20201016_02_T2
Landsat-8	2017-12-30	LC08_L1GT_182114_20171230_20201016_02_T2
Landsat-8	2018-01-08	LC08_L1GT_181114_20180108_20201016_02_T2
Landsat-8	2018-02-14	LC08_L1GT_184114_20180214_20201016_02_T2
Landsat-8	2018-03-11	LC08_L1GT_183114_20180311_20200901_02_T2
Landsat-8	2018-09-28	LC08_L1GT_182114_20180928_20200830_02_T2
Landsat-8	2018-10-05	LC08_L1GT_183114_20181005_20200830_02_T2
Landsat-8	2018-10-12	LC08_L1GT_184114_20181012_20201016_02_T2
Landsat-8	2018-10-14	LC08_L1GT_182114_20181014_20201016_02_T2
Landsat-8	2018-10-21	LC08_L1GT_183114_20181021_20201016_02_T2
Landsat-8	2018-11-29	LC08_L1GT_184114_20181129_20201016_02_T2
Landsat-8	2019-01-18	LC08_L1GT_182114_20190118_20201016_02_T2
Landsat-8	2019-02-19	LC08_L1GT_182114_20190219_20201016_02_T2
Landsat-8	2019-03-23	LC08_L1GT_182114_20190323_20200829_02_T2
Landsat-8	2019-10-01	LC08_L1GT_182114_20191001_20200825_02_T2
Landsat-8	2019-10-17	LC08_L1GT_182114_20191017_20201016_02_T2
Landsat-8	2019-10-31	LC08_L1GT_184114_20191031_20201016_02_T2
Landsat-8	2019-11-02	LC08_L1GT_182114_20191102_20201016_02_T2
Landsat-8	2019-12-02	LC08_L1GT_184114_20191202_20201016_02_T2
Landsat-8	2019-12-27	LC08_L1GT_183114_20191227_20201016_02_T2
Landsat-8	2020-01-28	LC08_L1GT_183114_20200128_20201016_02_T2
Landsat-8	2020-02-20	LC08_L1GT_184114_20200220_20201016_02_T2
Landsat-8	2020-02-22	LC08_L1GT_182114_20200222_20201016_02_T2
Landsat-8	2020-09-24	LC08_L1GT_183114_20200924_20201007_02_T2
Landsat-8	2020-10-01	LC08_L1GT_184114_20201001_20201007_02_T2
Landsat-8	2020-10-10	LC08_L1GT_183114_20201010_20201016_02_T2
Landsat-8	2020-10-19	LC08_L1GT_182114_20201019_20201105_02_T2
Landsat-8	2020-11-18	LC08_L1GT_184114_20201118_20210315_02_T2
Landsat-8	2020-12-22	LC08_L1GT_182114_20201222_20210310_02_T2
Landsat-8	2021-01-07	LC08_L1GT_182114_20210107_20210307_02_T2
Landsat-8	2021-01-12	LC08_L1GT_185114_20210112_20210308_02_T2
Landsat-8	2021-01-19	LC08_L1GT_186113_20210119_20210307_02_T2
Landsat-8	2021-02-06	LC08_L1GT_184114_20210206_20210302_02_T2
Landsat-8	2021-03-01	LC08_L1GT_185113_20210301_20210311_02_T2
Landsat-8	2021-03-17	LC08_L1GT_185114_20210317_20210328_02_T2
Landsat-8	2021-03-24	LC08_L1GT_186113_20210324_20210401_02_T2
Landsat-8	2021-04-02	LC08_L1GT_185113_20210402_20210408_02_T2
Landsat-8	2021-04-04	LC08_L1GT_183114_20210404_20210408_02_T2
Landsat-8	2021-09-20	LC08_L1GT_182114_20210920_20210924_02_T2
Landsat-8	2021-09-25	LC08_L1GT_185113_20210925_20210930_02_T2
Landsat-8	2021-10-02	LC08_L1GT_186113_20211002_20211013_02_T2
Landsat-8	2021-10-06	LC08_L1GT_182114_20211006_20211013_02_T2
Landsat-8	2021-10-20	LC08_L1GT_184114_20211020_20211026_02_T2
Landsat-8	2021-11-05	LC08_L1GT_184114_20211105_20211116_02_T2
Landsat-8	2021-11-07	LC08_L1GT_182114_20211107_20211117_02_T2
Landsat-8	2021-12-05	LC08_L1GT_186113_20211205_20211215_02_T2
Landsat-8	2021-12-25	LC08_L1GT_182114_20211225_20211230_02_T2
Landsat-9	2021-12-31	LC09_L1GT_184114_20211231_20220121_02_T2

Table 6. Halloween Crack width digitization along RGT 215 1LR, RGT 1160 3LR and RGT 786 2LR between the western pair of GNSS receivers from Landsat-8 and Landsat-9, used in Fig. 4.

Platform	Date	width (m) - opening width (wall-to-wall width)					
		1160 3L	1160 3R	215 1L	215 1R	786 2L	786 2R
Landsat-8	2017-11-12	221	220	224	223	192	195
Landsat-8	2017-12-21	241	240	251	246	223	220
Landsat-8	2017-12-30	246	245	268	252	232	225
Landsat-8	2018-01-08	260	255	259	247	243	244
Landsat-8	2018-02-14	269	275	270	267	272	268
Landsat-8	2018-03-11	296	294	283	293	284	281
Landsat-8	2018-09-28	475	464	404 (645)	401 (623)	475	456
Landsat-8	2018-10-05	477	472	427 (663)	420 (636)	483	462
Landsat-8	2018-10-12	484	485	435 (671)	439 (649)	500	478
Landsat-8	2018-10-14	485	490	442 (669)	455 (659)	497	476
Landsat-8	2018-10-21	493	507	442 (665)	446 (663)	494	483
Landsat-8	2018-11-29	498 (576)	544	490 (706)	494 (709)	532	526
Landsat-8	2019-01-18	536 (684)	552 (638)	513 (732)	513 (740)	568	576
Landsat-8	2019-02-19	527 (729)	576 (715)	534 (746)	530 (744)	602	597
Landsat-8	2019-03-23	538 (758)	584 (763)	558 (738)	543 (740)	607	605
Landsat-8	2019-10-01	676 (903)	681 (904)	653 (732)	667 (797)	799	785 (919)
Landsat-8	2019-10-17	697 (912)	685 (923)	685 (741)	681 (785)	788 (856)	815 (945)
Landsat-8	2019-10-31	687 (899)	720 (940)	682 (746)	770	836 (927)	783 (944)
Landsat-8	2019-11-02	704 (914)	720 (931)	701 (750)	774	821 (913)	780 (964)
Landsat-8	2019-12-02	747 (928)	713 (924)	772	761	835 (985)	803 (1007)
Landsat-8	2019-12-27	791 (950)	752 (947)	765	796	811 (966)	832 (1034)
Landsat-8	2020-01-28	799 (947)	815 (983)	808	805	860 (1038)	831 (1060)
Landsat-8	2020-02-20	819 (946)	813 (987)	838	826	871 (1084)	852 (1087)
Landsat-8	2020-02-22	824 (952)	805 (988)	838	832	863 (1083)	863 (1099)
Landsat-8	2020-09-24	993	979	979	990	979 (1170)	973 (1150)
Landsat-8	2020-10-01	992	992	982	993	986 (1172)	982 (1154)
Landsat-8	2020-10-10	1006	1000	1015	1012	1001(1184)	1001 (1171)
Landsat-8	2020-10-19	1015	1004	1026	1019	1020 (1194)	1047 (1184)
Landsat-8	2020-11-18	1046	1052	1077	1043	1064 (1214)	1063 (1200)
Landsat-8	2020-12-22	1068	1062	1104	1111	1094 (1223)	1071 (1157)
Landsat-8	2021-01-07	1077	1066	1104	1106	1094 (1210)	1074 (1149)
Landsat-8	2021-01-12	1100	1091	1127	1130	1092 (1202)	1075 (1140)
Landsat-8	2021-01-19	1108	1095	1114	1130	1108 (1202)	1080 (1139)
Landsat-8	2021-02-06	1082	1066	1101	1106	1130 (1198)	1081 (1130)
Landsat-8	2021-03-01	1101	1106	1121	1120	1047 (1115)	1110
Landsat-8	2021-03-17	1101	1096	1094	1106	1096	1105
Landsat-8	2021-03-24	1094	1099	1100	1100	1099	1085
Landsat-8	2021-04-02	1113	1093	1106	1095	1091	1084
Landsat-8	2021-04-04	1084	1088	1078	1082	1108	1077
Landsat-8	2021-09-20	1132	1126	1052	1066	1067	1050
Landsat-8	2021-09-25	1130	1127	1073	1071	1076	1073
Landsat-8	2021-10-02	1158	1139	1081	1089	1080	1082
Landsat-8	2021-10-06	1152	1145	1068	1069	1076	1083
Landsat-8	2021-10-20	1162	1154	1067	1080	1089	1094
Landsat-8	2021-11-05	1163	1166	1070	1085	1090	1118
Landsat-8	2021-11-07	1166	1171	1076	1080	1104	1127
Landsat-8	2021-12-05	1136	1172	1096	1087	1137	1152
Landsat-8	2021-12-25	1134	1179	1104	1096	1165	1186
Landsat-9	2021-12-31	1134	1164	1117	1107	1166	1210

Table 7. Halloween Crack width digitization along RGT 283 1LR, RGT 725 3LR and RGT 1099 2LR between the western pair of GNSS receivers from Landsat-8 and Landsat-9, used in Fig. 5.

Platform	Date	width (m) - opening width					
		283 1L	283 1R	725 3L	725 3R	1099 2L	1099 2R
Landsat-8	2017-11-12	123	138	164	131	191	172
Landsat-8	2017-12-21	172	166	181	151	203	194
Landsat-8	2017-12-30	171	175	179	162	209	204
Landsat-8	2018-01-08	174	193	174	153	195	222
Landsat-8	2018-02-14	207	189	189	171	203	209
Landsat-8	2018-03-11	193	203	185	178	200	209
Landsat-8	2018-09-28	272	279	392	310	291	289
Landsat-8	2018-10-05	288	289	380	324	304	310
Landsat-8	2018-10-12	305	318	359	337	305	308
Landsat-8	2018-10-14	303	313	370	340	305	309
Landsat-8	2018-10-21	316	331	361	344	313	318
Landsat-8	2018-11-29	335	332	372	341	318	323
Landsat-8	2019-01-18	414	443	351	341	351	331
Landsat-8	2019-02-19	485	475	367	370	357	334
Landsat-8	2019-03-23	465	481	367	362	349	367
Landsat-8	2019-10-01	452	439	456	488	445	450
Landsat-8	2019-10-17	459	452	472	491	464	451
Landsat-8	2019-10-31	438	444	457	471	455	452
Landsat-8	2019-11-02	472	464	488	495	462	474
Landsat-8	2019-12-02	479	481	502	509	480	482
Landsat-8	2019-12-27	478	481	516	491	483	501
Landsat-8	2020-01-28	490	510	506	496	506	507
Landsat-8	2020-02-20	506	507	508	482	508	515
Landsat-8	2020-02-22	513	527	501	492	520	522
Landsat-8	2020-09-24	586	565	691	730	579	578
Landsat-8	2020-10-01	597	574	723	747	595	581
Landsat-8	2020-10-10	604	585	727	782	604	588
Landsat-8	2020-10-19	605	592	770	780	614	590
Landsat-8	2020-11-18	621	569	774	791	623	618
Landsat-8	2020-12-22	633	651	799	786	650	651
Landsat-8	2021-01-07	641	667	780	800	669	667
Landsat-8	2021-01-12	635	684	807	724	683	688
Landsat-8	2021-01-19	640	674	796	756	674	681
Landsat-8	2021-02-06	653	714	802	794	664	670
Landsat-8	2021-03-17	761	775	694	664	608	664
Landsat-8	2021-03-24	770	801	694	647	595	674
Landsat-8	2021-04-02	760	793	659	631	564	645
Landsat-8	2021-04-04	760	795	645	629	562	673
Landsat-8	2021-09-20	693	643	616	614	713	690
Landsat-8	2021-09-25	679	657	624	614	702	665
Landsat-8	2021-10-02	687	663	640	631	684	688
Landsat-8	2021-10-06	682	671	635	637	688	718
Landsat-8	2021-10-20	673	682	650	637	692	723
Landsat-8	2021-11-05	685	689	640	645	667	698
Landsat-8	2021-11-07	670	686	647	657	665	689
Landsat-8	2021-12-05	693	678	668	662	643	684
Landsat-8	2021-12-25	694	668	666	672	640	653
Landsat-9	2021-12-31	697	652	676	655	623	620

Table 8. Sentinel-1 SAR and Sentinel-2 and Landsat-8 optical imagery used for ice flow modeling. Ice flow velocity was calculated by applying a feature tracking algorithm to Sentinel-1 SAR scene pairs separated by 12 days using the SeNtinel Applications Platform (SNAP). The model domain was defined using Sentinel-2 and Landsat-8 images.

Period	Sentinel-1 pair and Sentinel-2/Landsat-8 images
"Pre-calving"	S1A_IW_GRDH_1SSH_20200228T035038_20200228T035107_031447_039EDA_15B1 S1A_IW_GRDH_1SSH_20200311T035039_20200311T035107_031622_03A4ED_53C5 LC08_L1GT_184113_20200220_20201016_02_T2 LC08_L1GT_184114_20200220_20201016_02_T2
"Calving"	S1A_IW_GRDH_1SSH_20210318T035044_20210318T035113_037047_045C31_C4C6 S1A_IW_GRDH_1SSH_20210330T035045_20210330T035113_037222_04623E_9BAF S2B_MSIL2A_20210314T100059_N0214_R093_T26CNB_20210314T120106 S2B_MSIL2A_20210314T100059_N0214_R093_T26CNA_20210314T120106 S2B_MSIL2A_20210314T100059_N0214_R093_T26CMA_20210314T120106 S2B_MSIL1C_20210314T100059_N0209_R093_T26CMB_20210314T113145
"Post-calving"	S1A_IW_GRDH_1SSH_20211125T035053_20211125T035122_040722_04D518_F687 S1A_IW_GRDH_1SSH_20211207T035053_20211207T035121_040897_04DB2E_4704 LC08_L1GT_184113_20211020_20211026_02_T2 LC08_L1GT_184114_20211020_20211026_02_T2

Table 9. Inputs to *icepack* (diagnostic) inverse and additional diagnostic model runs and calculated HC opening rates. Inverse models take SNAP feature tracked velocity fields (Table S8) as initial-guess inputs, and output modeled velocity and fluidity fields. These outputs are used as inputs to the additional diagnostic model runs. HC opening rates between the western and eastern GNSS pairs are calculated as the difference in the rift perpendicular components of velocity north (N perp.) and south (S perp.) of the rift.

Model	Velocity	Fluidity	Geometry (extent/rift)	Temp. (K)	Western			Eastern		
					N perp. ($m\,a^{-1}$)	S perp. ($m\,a^{-1}$)	**rate** ($m\,a^{-1}$)	N perp. ($m\,a^{-1}$)	S perp. ($m\,a^{-1}$)	**rate** ($m\,a^{-1}$)
"pre-calving" Inverse	FT pre (output: model pre)	(output: model pre)	pre/pre	253	416.7	159.8	**257.0**	649.0	455.9	**193.1**
"calving" Inverse	FT calve (output: model calve)	(output: model calve)	calve/calve	253	227.7	174.1	**53.6**	505.1	468.7	**36.4**
"post-calving" Inverse	FT post (output: model post)	(output: model post)	post/post	253	327.9	191.4	**136.5**	605.2	517.6	**87.6**
Diagnostic$_1$	model pre	model pre	pre/pre	253	463.6	178.2	**285.4**	650.4	461.4	**189.0**
Diagnostic$_2$	model pre	model pre	calve/pre	253	461.8	174.1	**287.7**	658.1	459.1	**199.0**
Diagnostic$_3$	model pre	model pre	post/pre	253	497.9	179.2	**318.7**	671.6	468.9	**202.7**
Diagnostic$_4$	model pre	model pre	calve/calve	253	430.4	184.7	**245.7**	650.2	471.5	**178.7**
Diagnostic$_5$	model pre	model pre	post/post	253	428.9	180.3	**248.7**	659.6	467.4	**192.1**
Diagnostic$_6$	model calve	model pre	calve/pre	253	268.5	175.3	**93.2**	515.6	449.2	**66.4**
Diagnostic$_7$	model post	model pre	post/pre	253	417.3	157.6	**259.7**	635.1	469.0	**166.1**
Diagnostic$_8$	model calve	model pre	calve/calve	253	250.6	183.9	**66.7**	513.5	457.7	**55.8**
Diagnostic$_9$	model post	model pre	post/post	253	340.9	159.3	**181.5**	622.7	467.9	**154.8**
"pre-calving" Inverse	FT pre (output: model pre)	(output: model pre)	pre/pre	260	394.8	157.8	**237.0**	633.2	495.8	**137.4**
"calving" Inverse	FT calve (output: model calve)	(output: model calve)	calve/calve	260	226.2	175.6	**50.6**	504.0	475.7	**28.3**
"post-calving" Inverse	FT post (output: model post)	(output: model post)	post/post	260	326.2	193.0	**133.3**	603.1	524.8	**78.3**
Diagnostic$_1$	model pre	model pre	pre/pre	260	425.6	177.6	**248.5**	634.9	500.9	**134.0**
Diagnostic$_2$	model pre	model pre	calve/pre	260	415.3	180.6	**234.7**	625.1	506.6	**118.5**
Diagnostic$_3$	model pre	model pre	post/pre	260	514.1	184.6	**329.5**	642.9	520.3	**122.6**
Diagnostic$_4$	model pre	model pre	calve/calve	260	351.9	182.1	**169.7**	628.5	509.5	**119.0**
Diagnostic$_5$	model pre	model pre	post/post	260	335.7	176.7	**159.0**	638.0	500.5	**137.5**
Diagnostic$_6$	model calve	model pre	calve/pre	260	199.8	181.0	**18.8**	495.6	496.4	**-0.8**
Diagnostic$_7$	model post	model pre	post/pre	260	324.8	162.2	**162.7**	615.4	514.7	**100.7**
Diagnostic$_8$	model calve	model pre	calve/calve	260	182.5	187.9	**-5.4**	494.6	502.0	**-7.4**
Diagnostic$_9$	model post	model pre	post/post	260	251.9	160.7	**91.2**	604.6	503.7	**100.9**

References

Andersen, O. B. and Knudsen, P.: The DNSC08 mean sea surface and mean dynamic topography, Journal of Geophysical Research, p. C11, https://doi.org/10.1029/2008JC005179, 2009.

170 De Rydt, J., Gudmundsson, G. H., Nagler, T., Wuite, J., and King, E. C.: Recent rift formation and impact on the structural integrity of the Brunt Ice Shelf, East Antarctica, The Cryosphere, 12, 505–520, https://doi.org/10.5194/tc-12-505-2018, 2018.

Gardner, A. S., Moholdt, G., Scambos, T., Fahnstock, M., Ligtenberg, S., van den Broeke, M., and Nilsson, J.: Increased West Antarctic and unchanged East Antarctic ice discharge over the last 7 years, The Cryosphere, 12, 521–547, https://doi.org/10.5194/tc-12-521-2018, 2018.

Gardner, A. S., Fahnstock, M., and Scambos, T.: ITS_LIVE Regional Glacier and Ice Sheet Surface Velocities, Data archived at National 175 Snow and Ice Data Center, https://doi.org/10.5067/6II6VW8LLWJ7, 2020.

King, E. C., De Rydt, J., and Gudmundsson, G. H.: The internal structure of the Brunt Ice Shelf from ice-penetrating radar analysis and implications for ice shelf fracture, The Cryosphere, 12, 3361–3372, https://doi.org/10.5194/tc-12-3361-2018, 2018.

Morlighem, M.: MEaSUREs BedMachine Antarctica, Version 2. [floating ice mask, firn air content], Boulder, Colorado USA. NASA National Snow and Ice Data Center Distributed Active Archive Center, https://doi.org/10.5067/E1QL9HFQ7A8M, date Accessed: 2021, 180 2020.

Pavlis, N. K., Holmes, S. A., Kenyon, S. C., and Factor, J. K.: The development and evaluation of the Earth Gravitational Model 2008 (EGM2008), Journal of Geophysical Research: Solid Earth, 117, https://doi.org/10.1029/2011JB008916, 2012.

Swinski, J. P., Shean, D., and Sutterley, T.: ICESat2-SlideRule/sliderule-icesat2: v1.4.3, https://doi.org/10.5281/zenodo.6600555, 2022.